JGR Oceans

RESEARCH ARTICLE
10.1029/2018JC014820

Key Points:
- Ocean currents alter the climatological significant wave heights by as much as 0.18 m (±15%) in the Gulf of Mexico
- Swell energy constitutes an average of more than 30% of wave energy over the Gulf of Mexico
- The importance of surface gravity waves in ocean-atmosphere coupling is spatially and temporally variable in the Gulf of Mexico

Supporting Information:
- Supporting Information S1

Correspondence to:
J.-H. Liang,
jliang@lsu.edu

Citation:
Abolfazli, E., Liang, J.-H., Fan, Y., Chen, Q. J., Walker, N. D., & Liu, J. (2020). Surface gravity waves and their role in ocean-atmosphere coupling in the Gulf of Mexico. *Journal of Geophysical Research: Oceans*, *125*, e2018JC014820. https://doi.org/10.1029/2018JC014820

Received 29 NOV 2018
Accepted 8 JUN 2020
Accepted article online 10 JUN 2020

Surface Gravity Waves and Their Role in Ocean-Atmosphere Coupling in the Gulf of Mexico

Ehsan Abolfazli[1], Jun-Hong Liang[1,2,3], Yalin Fan[4], Qin Jim Chen[5], Nan D. Walker[1,3], and Jinliang Liu[1]

[1]Department of Oceanography and Coastal Sciences, Louisiana State University, Baton Rouge, LA, USA, [2]Center for Computation and Technology, Louisiana State University, Baton Rouge, LA, USA, [3]Coastal Studies Institute, Louisiana State University, Baton Rouge, LA, USA, [4]Oceanography Division, Naval Research Laboratory, Stennis Space Center, MS, USA, [5]Department of Civil and Environmental Engineering, Northeastern University, Boston, MA, USA

Abstract This study provides an overview of the surface gravity wave dynamics in the Gulf of Mexico (GoM) using numerical simulations. The focus is on the effects of ocean currents on waves, and the geographic distribution of wave statistics and parameters related to the role of waves on both sides of the ocean-atmosphere interface. Simulations are performed using the Simulating WAves Nearshore (SWAN) model with and without coupling with the Regional Ocean Modeling System (ROMS) model within the Coupled Ocean Atmosphere Wave Sediment Transport (COAWST) framework. In the GoM, currents alter the climatological significant wave heights by up to 0.18 m (±15%), reducing wave heights in the southwestern GoM and generally increasing wave heights in other regions. In two instantaneous snapshots representing the Loop Current variability in terms of its northward extension into the GoM, significant wave heights are modulated by as much as 0.30 m (±35%) by the currents. Probability density of wave height modulation covers a wider range of values and is skewed toward positive values over the eastern flank of the Loop Current. In winter, spring, and fall, swell fraction of wave energy increases from east to west in the GoM and reaches as high as 0.8 in the southwestern GoM, off the coast of Mexico. The dominance of swell in this region combined with weak wind results in a higher prevalence of the wave-driven wind regime throughout the year. The interannual variability of significant wave height and swell fraction shows signals of major storms in the GoM.

Plain Language Summary The Gulf of Mexico (GoM) is a marginal sea that provides many critical resources for the United States, Mexico, and Cuba. Waves at the ocean surface play an important role in the GoM. These waves are significantly affected by ocean currents. Major ocean currents in the GoM include the Loop Current, which enters the GoM from the Yucatan channel and leaves through the Strait of Florida, and westward-propagating eddies that are circular currents spanning a hundred kilometers or so. Our results show that mean wave heights are altered by up to 0.18 m (±15%) by currents in the GoM. The wind waves away from their origin, called swell, are substantial in summer in the northern GoM and in the southwestern GoM. They are able to drive the wind. The wind and the waves can also affect the mixing in the upper ocean differently across seasons and locations in the GoM, implying that their roles should be explicitly accounted for in computational ocean models.

1. Introduction

The Gulf of Mexico (GoM) is a semienclosed marginal sea surrounded by the North American continent and Cuba. It provides abundant physical and biological resources, supporting a variety of industries such as fisheries, energy, and tourism in the United States, Mexico, and Cuba. It is also on the path of many major North Atlantic hurricanes that erode and resuspend sediments (e.g., Xu et al., 2016), cool the ocean surface (e.g., Shay et al., 2000), fuel phytoplankton blooms (e.g., Liu et al., 2019a; Walker et al., 2005), and alter the distribution of dissolved organic matters (e.g., Liu et al., 2019b). The major surface current in the GoM is the Loop Current, which is an integral part of the western boundary current. The Loop Current links the Yucatan Current entering the GoM from the Caribbean Sea to the Florida Current within the Florida Straits. It also modulates the outbreak of harmful algal bloom in the West Florida Shelf (WFS) by

interacting with the shelf break (Liu, Weisberg, Lenes, et al., 2016). The Loop Current exhibits strong variability, alternating between northward penetration and southward retreat. When it retreats, anticyclonic eddies pinch off from the Loop Current and propagate westward. Transport through the Florida Strait (Sturges et al., 2010), the intensity of Yucatan undercurrent (Bunge et al., 2002), and prior closed circulation within the Loop Current (Forristall et al., 1992) are among the factors that have been proposed to affect the Loop Current extension and the shedding of mesoscale eddies called the Loop Current rings. Circulation in the GoM and its seasonal and interannual variability have been extensively studied using observations and computer models (e.g., Alvera-Azcárate et al., 2009; He & Weisberg, 2003; Liu, Weisberg, Vignudelli, et al., 2016; Oey et al., 2013; Sturges & Leben, 2000; Vukovich, 2007).

Ocean surface gravity waves in the GoM have received less attention compared to other parameters that describe the state of the oceans such as temperature, salinity, chlorophyll-*a*, and currents. In this study, we, therefore, aim to examine the mean and the variability of surface wave characteristics in the GoM. Surface gravity waves are important for navigation, offshore structure design, coastal erosion, and the coupling between the ocean and the atmosphere. They are comprised of locally generated wind seas and remotely generated swells. As indicated by its name, the wind supplies energy for the wind wave growth, while whitecapping, depth-induced wave breaking, and bottom friction drain energy from the waves and cause them to decay. When wind waves leave their generation zone and no longer get energy from the local winds, they are considered swells. Swells can be very persistent and travel thousands of kilometers before they dissipate. Currently, there is no consensus on the cause of swell dissipation (The WISE Group, 2007). Possible reasons include interaction with ocean turbulence (Babanin, 2011) or interaction with airflow to create wave-driven winds (Harris, 1966).

The evolution and fate of surface gravity waves are affected by the ocean currents over which waves travel. Currents can induce shoaling and refraction and cause Doppler shift in the frequency of the waves (e.g., Wolf & Prandle, 1999). Currents can also indirectly affect the waves by changing the velocity of the surface wind relative to the surface water, which alters the wind energy input to waves (Warner et al., 2010). These currents effects change the wave energy spectrum and the spatial and temporal distribution of wave characteristics including height and direction. Early studies (e.g., Holthuijsen & Tolman, 1991; Wang et al., 1994) focus on the effect of large-scale currents at scales similar to those of the Loop Current and the eddies detaching from it (e.g., Donohue et al., 2016; Liu, Weisberg, Vignudelli, et al., 2016; Sturges & Leben, 2000). Recent studies (e.g., Ardhuin et al., 2017) demonstrate that meso and submesoscale ocean currents (10 to 100 km) also modulate the wave characteristics and control the variability of wave height at meso and submesoscale scales. Wave height modulation due to the shoaling effect can be estimated by the conservation of wave action as $H_s/H_{s0} = \sqrt{\sigma C_{g0}/\left(\sigma_0\left(C_g + U_c\right)\right)}$ (e.g., Ardhuin et al., 2012) where H_s is significant wave height, σ is the radian frequency, C_g is the group velocity, and U_c is the current speed, and subscript "0" denotes the case without the current effect. For a typical current speed of 1 m/s (e.g., DiMarco et al., 2005) and a wave period of 6 s (e.g., Appendini et al., 2013), H_s can be modulated between −17% and +30%. Considering that H_s scales with U_{10}^2 in wind seas (Holthuijsen, 2010), the modulation of H_s by the relative wind speed effect can be estimated as $\pm 2U_c/U_{10}$ (e.g., Gemmrich & Garrett, 2012) where U_{10} is the 10-m wind speed. Considering a typical mean wind speed of 7 m/s in the GoM (e.g., Appendini et al., 2013) and a typical Loop Current speed of 1 m/s, the relative wind effect can amount to ±28%. The current effect on wave has been studied in a few regional oceans and estuaries, such as the Southern California Bight (Cao et al., 2018), the southwest Western Australian continental Shelf (Wandres et al., 2017), the northern GoM close to the coast of Alabama (Romero et al., 2017), the Delaware Bay and the adjacent continental shelf (Kukulka et al., 2017), the northern Mobil Bay (Chen et al., 2005), and the Barataria Pass of the northern GoM (Sorourian et al., 2020). Those studies report that currents alter significant wave height by up to 20% to 50%.

Waves are driven by the wind and transfer momentum and energy to the ocean when they break (Melville, 1996). Observations have shown that surface waves can also drive the wind (Grachev & Fairall, 2001) when remotely generated swells propagate substantially faster than the calm local wind. Inclusion of swell effects on the wind stress and atmosphere mixing has been shown to improve simulated wind speeds (Wu et al., 2016). This makes waves an important factor in mediating the air-sea momentum transfer. The degree of coupling between waves and the overlying atmosphere can be quantified by wave

age. Wave age is a dimensionless measure of characteristic wave speed relative to wind speed. It was defined and used in multiple forms in the literature, e.g., c_p/U_{10} (e.g., Högström et al., 2009), $c_p/U_{10}cos\Delta\theta$ (e.g., Hanley et al., 2010), and c_p/u_* (e.g., Drennan et al., 2003), where c_p is peak wave phase speed, $\Delta\theta$ is the angle between waves and the wind, and u_* is wind friction velocity. For the purpose of quantifying the degree of coupling between waves and overlying atmosphere, we adopt the form for wave age (W_{age}) used in Grachev and Fairall (2001) and Hanley et al. (2010):

$$W_{age} = \frac{c_p}{U_{10}cos\Delta\theta}. \tag{1}$$

Based on the observation by Högström et al. (2009) and Smedman et al. (2009) that wind profile and turbulent kinetic energy are similar in swell conditions for different wind-wave misalignments ($\Delta\theta$), Högström et al. (2011) proposed the use of c_p/U_{10} rather than $c_p/U_{10}cos\Delta\theta$ for the calculation of wave age. However, because a criterion by Grachev and Fairall (2001) based on $c_p/U_{10}cos\Delta\theta$ to characterize the sign reversal of air-sea momentum flux is used to identify the wind-driven wave and wave-driven wind regimes in the GoM, the term $cos\Delta\theta$ is retained in our calculations. The wind-driven wave regime is identified by inverse wave age larger than 0.83, while the wave-driven wind regime is characterized by inverse wave age smaller than 0.15 (Hanley et al., 2010). Using the wave age criterion, Hanley et al. (2010) identified a prevalent wind-driven wave regime in regions such as the Southern Ocean and the Northern Hemisphere storm tracks, and a prevalent wave-driven wind regime in regions such as the tropical eastern ocean basin, off the coast of Southern California. In addition to air-sea momentum transfer, the distribution of breaking waves is also commonly characterized by wave age (e.g., Sutherland & Melville, 2013, 2015). There are more frequent large breaking waves during wind sea when wave age is small. Breaking waves mediate air-sea interaction. Therefore, wave age is also a parameter determining the energy flux from waves to ocean (e.g., Terray et al., 1996), the subsurface distribution of gas bubbles (e.g., Liang, McWilliams, Sullivan, et al., 2012), and the role of gas bubbles on air-sea gas transfer (e.g., Brumer et al., 2017; Deike & Melville, 2018; Liang et al., 2017). The significance of wave age in quantifying these processes makes it important to understand its spatial and temporal distribution over the GoM.

Surface gravity waves induce Stokes drift that changes the near-surface currents through the Stokes-Coriolis effect (Polton et al., 2005). They also play an important role in vertical mixing in the ocean surface boundary layer (OSBL) by driving Langmuir circulations through interaction with currents. Vertical mixing not only mediates the exchange of momentum, heat, and trace materials between the ocean interior and the atmosphere, but also modulates horizontal transport and dispersion by controlling the vertical profiles of horizontal currents, material concentrations, and temperature in the OSBL (e.g., D'Asaro et al., 2014; Liang et al., 2018). A number of studies (e.g., Fan et al., 2018; Kukulka et al., 2013; Rabe et al., 2015) demonstrate that simulated mixed layer temperature, mixing layer depth, and turbulence kinetic energy are consistent with the observations only when Langmuir circulation is included in the model. These findings are generic to all ocean regions and suggest that wind speed alone is not sufficient to quantify mixing in the upper ocean. Existing parameterizations for Langmuir circulation include the Langmuir number (e.g., Li et al., 2016; McWilliams & Sullivan, 2000; Van Roekel et al., 2012), highlighting the significance of calculation of Langmuir number as a parameter critical in mixing in the upper ocean. The Langmuir number (La) can be calculated as (McWilliams et al., 1997)

$$La = \sqrt{\frac{u^*}{u_{st}}}, \tag{2}$$

where u_{st} is the surface Stokes drift magnitude. Theoretically, Langmuir number is the ratio between turbulent kinetic energy production by current shear and that by the Stokes drift shear in the OSBL. A large La implies the greater contribution of wind-driven mixing, while a small La indicates the greater contribution of wave-driven mixing in the OSBL. Since most ocean models do not incorporate a parameterization for Langmuir circulations, knowledge of the mixing effect of waves in the GoM is beneficial to understanding potential biases in ocean model solutions for the GoM.

Existing studies on surface gravity waves in the GoM primarily focus on wave characteristics during individual extreme events such as hurricanes (e.g., Hu & Chen, 2011; Huang et al., 2013; Sheng et al., 2010). To the best of our knowledge, there have been only two studies devoted to the long-term investigation of surface gravity waves in the GoM region (Appendini et al., 2013, 2018). The former examined the long-term trend of wave heights, and the latter identified the Norte events in the GoM and estimated wave power during these events. The distributions of swell fraction, wave age, and Langmuir number and the effect of currents on waves have not been studied in the GoM.

We focus on parameters that describe the waves such as significant wave height and swell fraction, as well as a number of wave-related parameters important in air-sea coupling and ocean mixing such as wave age and Langmuir number over the GoM. The effects of currents on surface gravity waves are also studied. The objectives are achieved by analyzing a 10-year (2001 to 2010) numerical simulation using a wave model coupled with a circulation model. The remainder of this paper is organized as follows. Section 2 describes the models, the way they are configured, and the data used for model skill assessment. Section 3 validates the models using in situ buoy data, as well as altimetry data. Section 4 discusses the wave climate in the GoM. Section 5 focuses on the currents effects on waves. Section 6 discusses the parameters important in ocean-atmosphere coupling and wave-driven mixing. Section 7 is a summary.

2. Data and Methods

2.1. Model Description and Configuration

Simulations are carried out using the ocean and the wave modules in the Coupled Ocean Atmosphere Wave Sediment Transport (COAWST v3.3) modeling framework (Warner et al., 2010). The ocean module is based on the Regional Ocean Modeling System (ROMS subversion 885) model (Shchepetkin & McWilliams, 2005), and the wave module is based on the Simulating WAves Nearshore (SWAN v41.20) model (Booij et al., 1999).

2.1.1. SWAN Model

2.1.1.1. SWAN Spectral Wave Model Description

The SWAN model is a spectral wave model based on the wave action balance equation (The SWAN Team, 2011)

$$\frac{\partial N}{\partial t}+\frac{\partial C_x N}{\partial x}+\frac{\partial C_y N}{\partial y}+\frac{\partial C_\sigma N}{\partial \sigma}+\frac{\partial C_\theta N}{\partial \theta}=\frac{S_{tot}}{\sigma}, \tag{3}$$

where $N = E/\sigma$ is wave action density; E is wave energy density; t is time; θ is the wave direction; and C_x, C_y, C_σ, and C_θ are the propagation velocities in the x, y, σ, and θ spaces, respectively. The wave energy propagation velocity equals the sum of wave group velocity and current velocity (The SWAN Team, 2011)

$$C_x = C_{g,x} + U_x, \tag{4a}$$

$$C_y = C_{g,y} + U_y, \tag{4b}$$

where $C_{g,x}$ and $C_{g,y}$ are the waves group velocity components, and U_x and U_y are the surface ocean current velocity components, along the x and y directions, respectively. On the right-hand side of Equation 3, the source and sink terms (S_{tot}) include the effects of generation by the wind, dissipations by whitecapping, bottom friction, and depth-induced breaking, and nonlinear wave-wave interactions. The SWAN model has been used in various geographic locations and met-ocean conditions (e.g., Akpınar & Bingölbali, 2016; Collins et al., 2015; Huang et al., 2013; Kukulka et al., 2017; Rogers et al., 2007).

For the purpose of this study, two quantities, namely, swell energy and Stokes drift, are added as additional model outputs.

Stokes drift refers to the wave-phase-averaged Lagrangian velocity in the direction of ocean surface gravity waves (Stokes, 1847). Based on the linear wave theory, the vertical profile of Stokes drift is related to the wave energy spectrum (Kenyon, 1969):

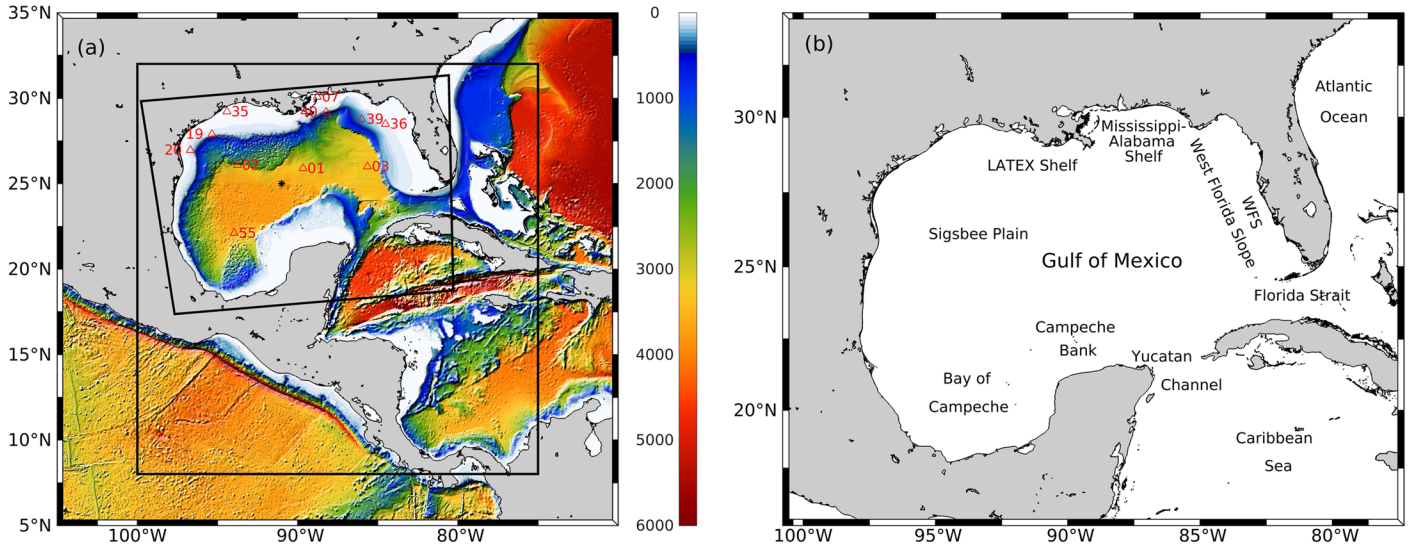

Figure 1. (a) Main model domain (smaller box), the domain used to validate the assumption of closed boundaries for SWAN (larger box), bathymetry (m) (color), and location and code of the NDBC buoys. Only the last two digits of buoy codes are shown as they all start with "420," and (b) a simple geography of the Gul of Mexico. (LATEX Shelf = Louisiana-Texas Shelf; WFS = West Florida Shelf).

$$\vec{u}_{st} = g\int_0^{2\pi}\int_0^{\infty}(cos\theta, sin\theta, 0)\frac{\vec{k}}{\sigma}\frac{2kcosh2k(z+h)}{\sinh 2kh}E(\sigma,\theta)dkd\theta, \tag{5}$$

where $\vec{u}_{st}$ denotes the surface Stokes drift vector, g is the gravitational acceleration, $\vec{k}$ is the wavenumber vector, k is the magnitude of the wavenumber vector, z is vertical coordinate, and h is depth. With the assumption of deep water waves, Equation 5 reduces to (e.g., Webb & Fox-Kemper, 2011):

$$\vec{u}_{st} = \frac{2}{g}\int_0^{2\pi}\int_0^{\infty}(cos\theta, sin\theta, 0)\sigma^3 E(\sigma,\theta)d\sigma d\theta. \tag{6}$$

The original algorithm in SWAN for identifying swell is based on an arbitrary choice of a cut-off frequency such that the spectral bins with frequencies smaller than the cut-off frequency are considered to constitute swells. This approach does not take into account the relative magnitudes of the wave phase speed and the overlying wind speed nor the wind-wave misalignment. We, therefore, modified the original SWAN code based on the Wave Spectral Energy Partitioning (WaveSEP) method by Tracy et al. (2007) to separate the directional wave spectrum into wind seas and swells. In this method, the wave components traveling at phase speeds slower than U_P are considered to be wind seas

$$U_P = C_{mult}U_{10}\cos(\theta - \theta_{wind}), \tag{7}$$

where U_P is the wind component in the wave direction and includes a wave age factor C_{mult} with a default value of 1.7, and θ_{wind} denotes the direction of the 10-m wind. The same value for C_{mult} is used in the WAVEWATCH III model (Tolman, 2009) and is shown to give reasonable swell energy estimates (Hanson et al., 2009).

2.1.1.2. SWAN Model Configuration

The computational domain encompasses the GoM (Figure 1a, smaller box) with a horizontal resolution of 0.05° × 0.05°. The bathymetry of the model (Figure 1b) is obtained from the ETOPO2v2 database (Smith & Sandwell, 1997). The wave model is forced by the wind from 3-hourly NCEP Climate Forecast System Reanalysis (CFSR) product (Saha et al., 2010) with a spatial resolution of 0.312° × 0.312°. The simulations are conducted over a 12-year period from 1999 to 2010, over which the CFSR data are continuously available. The first 2 years of the simulation are used to spin up the model and are excluded from the analysis.

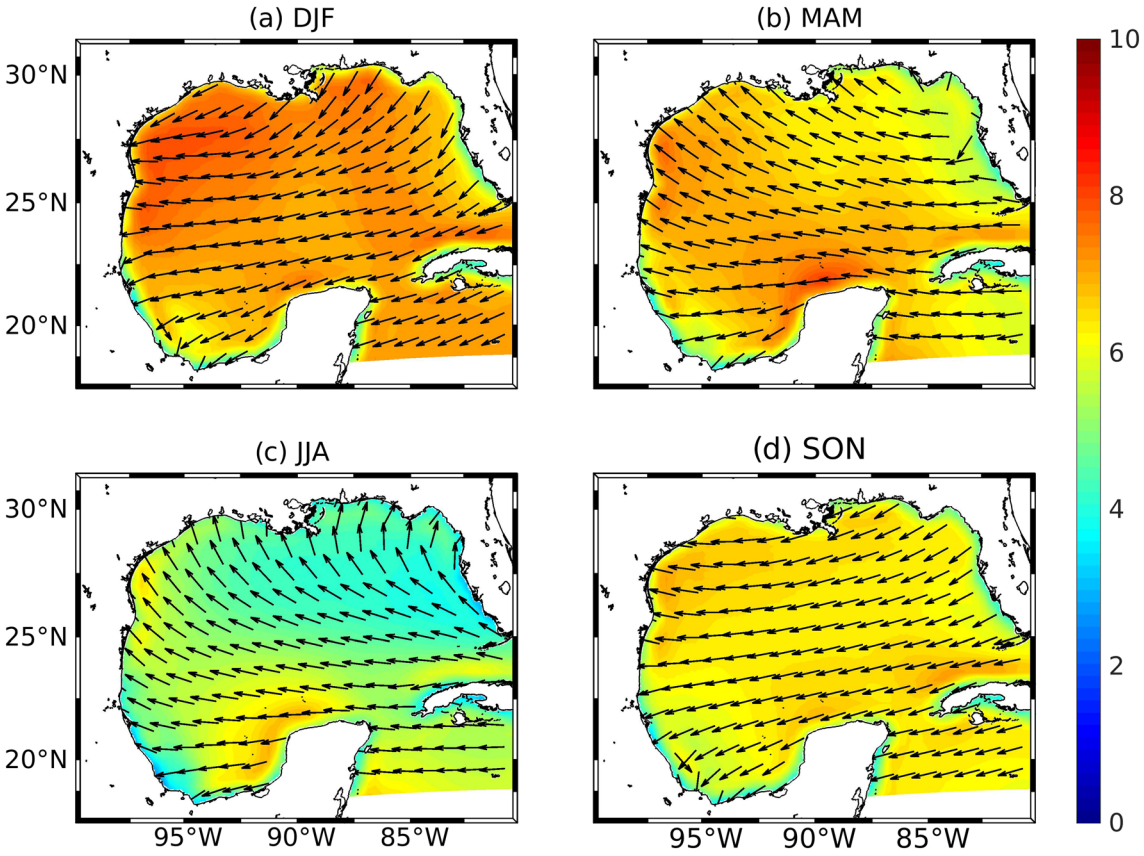

Figure 2. Seasonal climatology of 10-m wind speed (m/s) (color) and direction (arrows) over the years 2001–2010 based on CFSR wind data for (a) December–February (DJF), (b) March–May (MAM), (c) June–August (JJA), and (d) September–November (SON).

The 10-m wind is predominantly directed westward over the GoM as part of the trade winds (Figures 2a–2d). There is clear seasonal variability in the mean U_{10} with the strongest winds during winter (Figure 2a) and the weakest winds during summer (Figure 2c). The strongest climatological winter winds (>8.5 m/s) occur over the northwestern GoM. In summer, the lowest U_{10} (Figure 2c) occurs close to the western coast of Florida (<3.5 m/s). Over a major part of the GoM away from the coasts, the mean U_{10} ranges from 3.5 to 8.5 m/s between summer and winter.

In the SWAN model, the eastern and southern boundaries are closed. A model with a similar setup but with an extended domain (Figure 1a, larger box) yielded almost identical results at the studied buoys over the GoM (supporting information Figure S1), showing the insignificant influence by the limited swells traveling into the GoM from the Atlantic Ocean and the Caribbean Sea. Forty-five-minute time steps are used in the SWAN model. Sensitivity tests show that further reduction in time step has little effect on results. The directional resolution is 10°, with a total of 36 directions. The lowest and highest frequencies in the wave spectrum are set to 0.0335 and 1 Hz, respectively, spaced logarithmically in 25 frequency bins.

2.1.2. ROMS Model

2.1.2.1. ROMS Model Description

Circulation in the GoM is simulated using ROMS. The ROMS model solves the hydrostatic primitive equations in vertical terrain-following coordinates and horizontal curvilinear grids with innovative algorithms for advection, mixing, pressure gradient, vertical-mode coupling, time stepping, and parallel efficiency. The K-profile parameterization is used for the vertical mixing effect by boundary layer turbulence (Large et al., 1994).

2.1.2.2. ROMS Model Configuration

The ROMS model uses the same horizontal grid with a horizontal resolution of 0.05° × 0.05° as the SWAN model does. Vertically, the grid has 40 terrain-following layers. Monthly climatologies of salinity,

temperature, currents, and sea surface height from the Simple Ocean Data Assimilation ocean/sea ice reanalysis (SODA) (Carton & Giese, 2008) are used at the open boundaries. The wind forcing for the ROMS model is derived from the CFSR product, the same as that for the SWAN model.

2.1.3. Model Coupling

Due to the intensive feedbacks between the ocean and the surface waves, many theoretical approaches (e.g., Ardhuin et al., 2004; McWilliams et al., 2004; Mellor, 2003) and implementations (e.g., Ardhuin et al., 2017; Chen et al., 2013; Kumar et al., 2012; Uchiyama et al., 2010) have been proposed for the coupling of the three-dimensional ocean circulation with waves (Bennis et al., 2011). In COAWST, the SWAN and the ROMS models are coupled using the Model-Coupling Toolkit (Larson et al., 2005). The spatially and temporally variable free surface elevation and current fields computed by ROMS are passed to SWAN at user-specified intervals (45-min intervals are used here) (Warner et al., 2010). In COAWST, computation of the current field $\left(\vec{U}_C = \left(U_x, U_y\right)\right)$ that is passed to SWAN from ROMS is based on the approach by Kirby and Chen (1989).

In a coupled ROMS-SWAN simulation, currents affect the wave action balance by both changing the group velocities (Equations 4a and 4b) and modifying the energy flux from the wind to waves through altering the relative speed between the wind and the surface water (Warner et al., 2010). Accordingly, energy flux from the atmosphere to the waves is calculated based on a relative wind velocity $(\Delta\vec{U})$, which is calculated as (Warner et al., 2010)

$$\Delta\vec{U} = \vec{U}_{10} - \vec{U}_C, \tag{8}$$

where $\Delta\vec{U}$ is 10-m wind velocity vector $(\vec{U}_{10})$ relative to ocean currents.

To assess the effects of currents on waves, a second simulation with similar configuration is conducted that does not include the currents effects on waves and has only the SWAN module activated within the COAWST framework (hereafter the SWAN-only simulation).

2.2. Observational Data Sets

Satellite altimetry and buoy data sets are used to assess the skill of the model. Buoy data are provided by the National Data Buoy Center (NDBC). Along-track quality-controlled satellite altimeter-derived H_s data are from IFREMER. Mean dynamic topography (MDT) data available at the 0.25° × 0.25° resolution are provided by AVISO. Delayed time level-4 sea level anomaly (SLA) data from multimission altimetry observations available at the 0.25° × 0.25° resolution are provided by Copernicus Marine Environment Monitoring Service.

3. Model Validation

The solutions from the coupled simulation are validated against in situ measurements from 11 buoys operated by NDBC, as well as satellite altimetry data.

3.1. SWAN Model Skill Assessment

The H_s time series at buoy stations 42001, 42002, 42003, 42007, 42019, 42020, 42035, 42036, 42039, 42040, and 42055 (see Figure 1a for their locations) are used in the assessment of the SWAN solution in the coupled simulation. These buoys cover both the open ocean and the coastal ocean and have a long history of observations over the GoM. The simulated H_s values compare well with in situ measurements (Figure 3). The Pearson correlation coefficients between the simulation and observation over the 10-year analysis period are larger than 0.90, and the absolute bias values between the simulation and observation are smaller than 7 cm (Figure 3).

In addition to bias and correlation coefficient, the Brier skill score (BSS) is used to assess the wind and the simulated H_s during the entire simulation period. To further examine the effects of sea state in terms of being in wind sea- and swell-dominated conditions on the skill score, the skill score for H_s is also separately calculated during these conditions (Table 1). The BSS is calculated as (e.g., Murphy & Epstein, 1989)

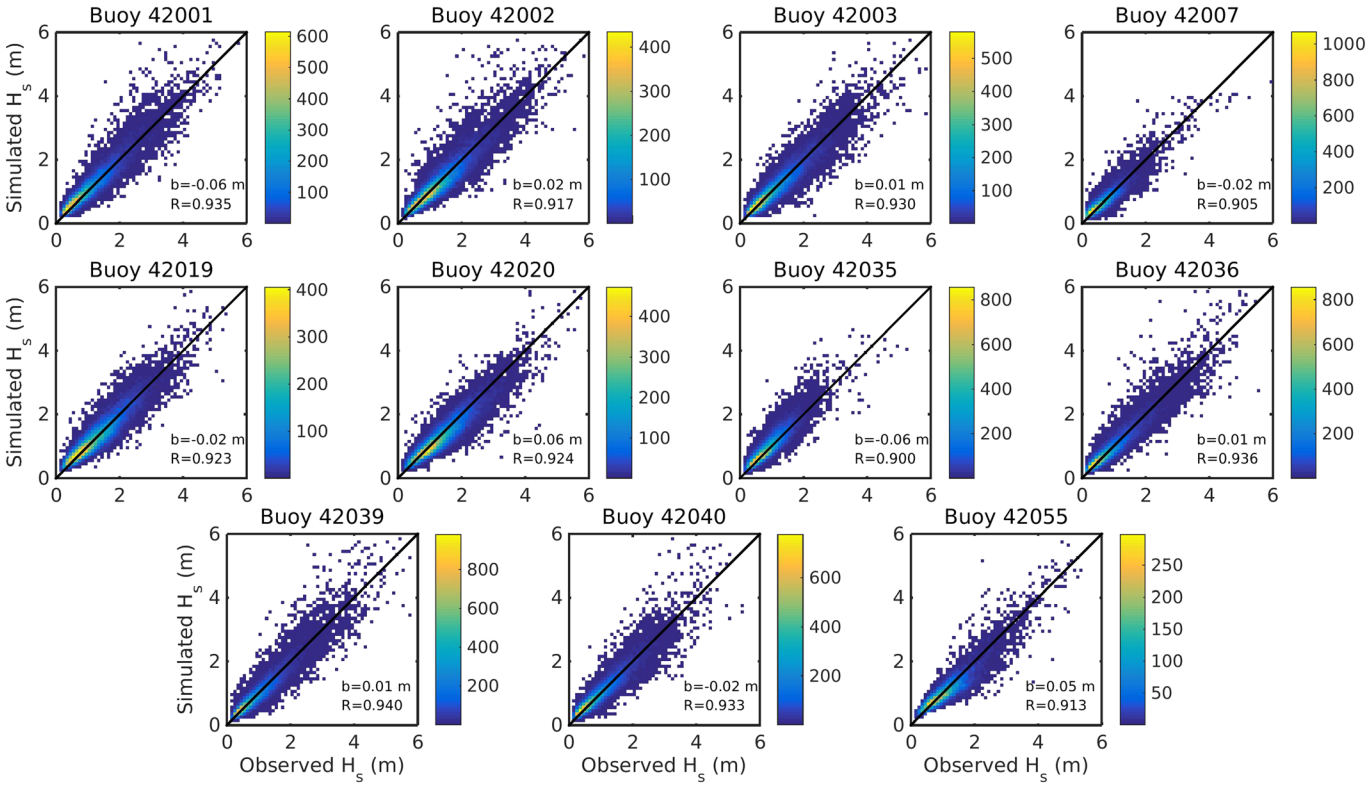

Figure 3. Scatter plots of simulated H_s (m) against buoy observations at 11 NDBC-operated buoys located in the GoM. Colors indicate the number of observations. The values b and R represent the bias and Pearson correlation coefficient between the simulated and observed H_s. The black line represents the 1:1 line. Comparison is based on the entire analysis period for all the data that were available for each buoy in that period.

$$BSS = 1 - \frac{\sum_{i=1}^{n}(x_i - y_i)^2}{\sum_{i=1}^{n}(x_i - c_i)^2}, \tag{9}$$

where n denotes the number of data points; x_i and y_i are the i_{th} observed and simulated values, respectively; and c_i is the long-term climatological mean of the observed time series. The skill score for H_s is greater than 0.82 at all buoy locations. In nine out of 11 buoys, the model performs better for wind seas. The model performs better in swell-dominated condition at buoys 42007 and 42035. These two buoys are located in the coastal regions, where the misrepresentation of the wind forcing is likely the cause of lower skill when the wind seas are dominant. This is also evident in the U_{10} skill scores, for which BSS is relatively small at buoys 42007 and 42035.

In addition to significant wave heights, the simulated direction-integrated wave energy spectrum, $\phi(f) = \int_0^{2\pi} E(f,\theta)d\theta$, agrees well with observations (Figure 4). Here f is the wave frequency in Hz and can be written as $f = \omega/2\pi$, where ω is the absolute radian frequency. Simulated (Figure 4b) and observed (Figure 4a) one-dimensional energy spectra agree well. Although there are differences between the simulated and the observed peak frequencies particularly during a number of periods in the month of June (Figure 4c), the model is able to capture the observed

Table 1
Skill Scores for Total H_s, Wind Sea H_s, Swell H_s, and U_{10}

Buoy	42,001	42,002	42,003	42,007	42,019	42,020	42,035	42,036	42,039	42,040	42,055
Total H_s	0.87	0.84	0.87	0.83	0.84	0.85	0.82	0.88	0.88	0.87	0.82
Wind sea H_s	0.85	0.84	0.83	0.80	0.83	0.86	0.75	0.86	0.87	0.86	0.79
Swell H_s	0.84	0.71	0.83	0.84	0.80	0.81	0.83	0.83	0.85	0.83	0.73
U_{10}	0.73	0.69	0.73	0.66	0.75	0.69	0.63	0.78	0.78	0.76	0.65

Note. The score is calculated using Equation 9. Locations of the buoys are shown in Figure 1.

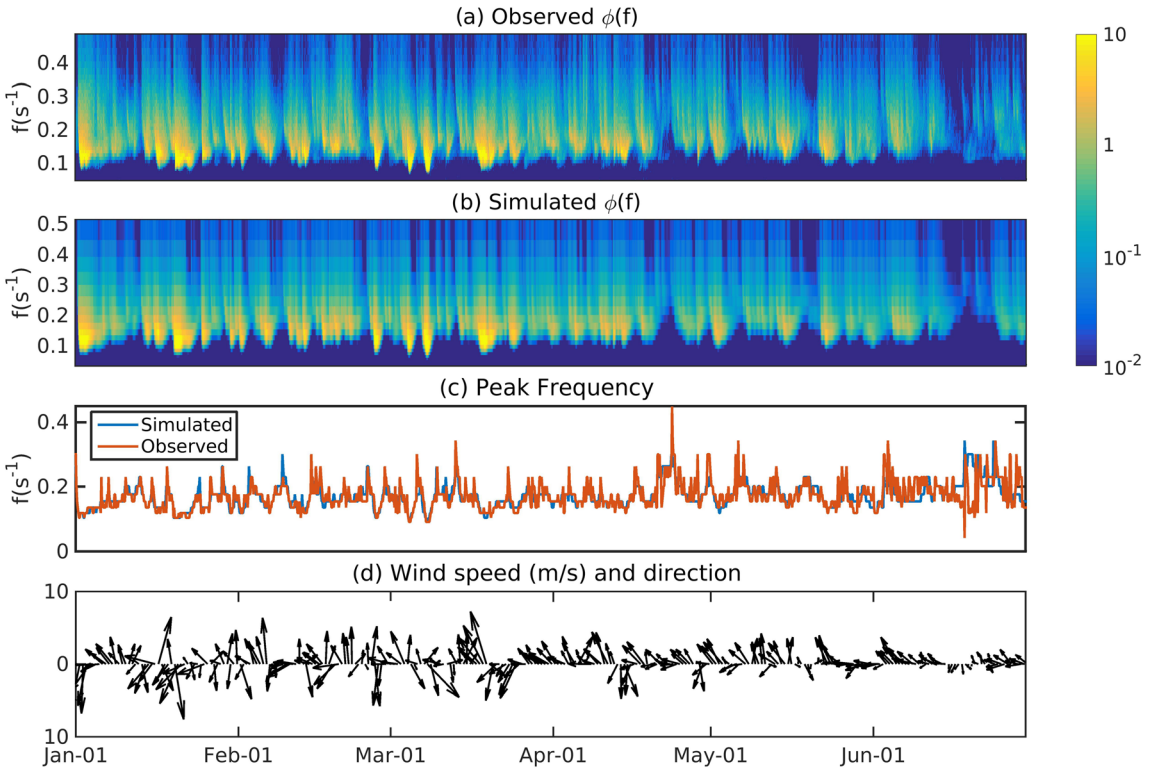

Figure 4. (a) Observed and (b) simulated direction-integrated energy spectrum $\Phi(f)$ (m^2/s), (c) observed and simulated peak frequency (Hz), and (d) wind speed and direction during January–June 2008 for buoy 42001.

spectral peaks and their changes both quantitatively and qualitatively. The frequency downshifts can be an indication of a sustained wind condition and a developing sea, while frequency upshifts can be due to a recent change in the wind direction. The energy density at spectral peaks is smaller in both the observation (Figure 4a) and the simulation (Figure 4b) during April–June, which is due to the smaller wind energy input to the waves when the wind is weaker (Figure 4d). Although the comparison shown here is for buoy 42001 during a randomly chosen period of January–June 2008, comparisons for other sample time periods and buoy selections yield similar conclusions. To assess the model performance using a different set of data, model solutions are also compared to satellite altimeter-derived H_s (Figure S2), which shows a good agreement. There is also a reasonably good comparison between the buoy-measured and altimeter-derived H_s during the analysis period (Figure S3).

3.2. Validation of the ROMS Model

Sea surface height and SLA are used to characterize the mean geostrophic currents (e.g., the Loop Current) and mesoscale variabilities (e.g., the Loop Current eddies). The mean sea surface height and the standard deviation of the high-frequency SLA from the ROMS model (Figures 5a and 5c) compare reasonably well with those from satellite altimetry data (Figures 5b and 5d), implying that the model is able to successfully capture the mean and mesoscale variability of geostrophic currents in the GoM. The high-frequency SLA is obtained by removing the long-term mean, annual cycle, 120-day running mean and 90-day running mean (see Liang et al., 2009; Liang, McWilliams, Kurian, et al., 2012, for details) so that only mesoscale variability is retained. The evident water mass with higher mean sea surface heights represents the region enclosed by the Loop Current (Figures 5a and 5b) with its location coinciding in the simulated and the observed maps. The slight westward extension of the Loop Current compared to observation is likely due to the reconnection of separated eddies (Figure 5a). The persistent anticyclonic feature in Figures 5a and 5b over the western GoM is one (or more) warm-core ring(s) separated from the Loop Current (Sturges & Kenyon, 2008). The strong variability in the high-frequency SLA in the northern parts of the Loop Current is likely associated with the fluctuation of the Loop Current, which occasionally extends close to the Louisiana-Texas and

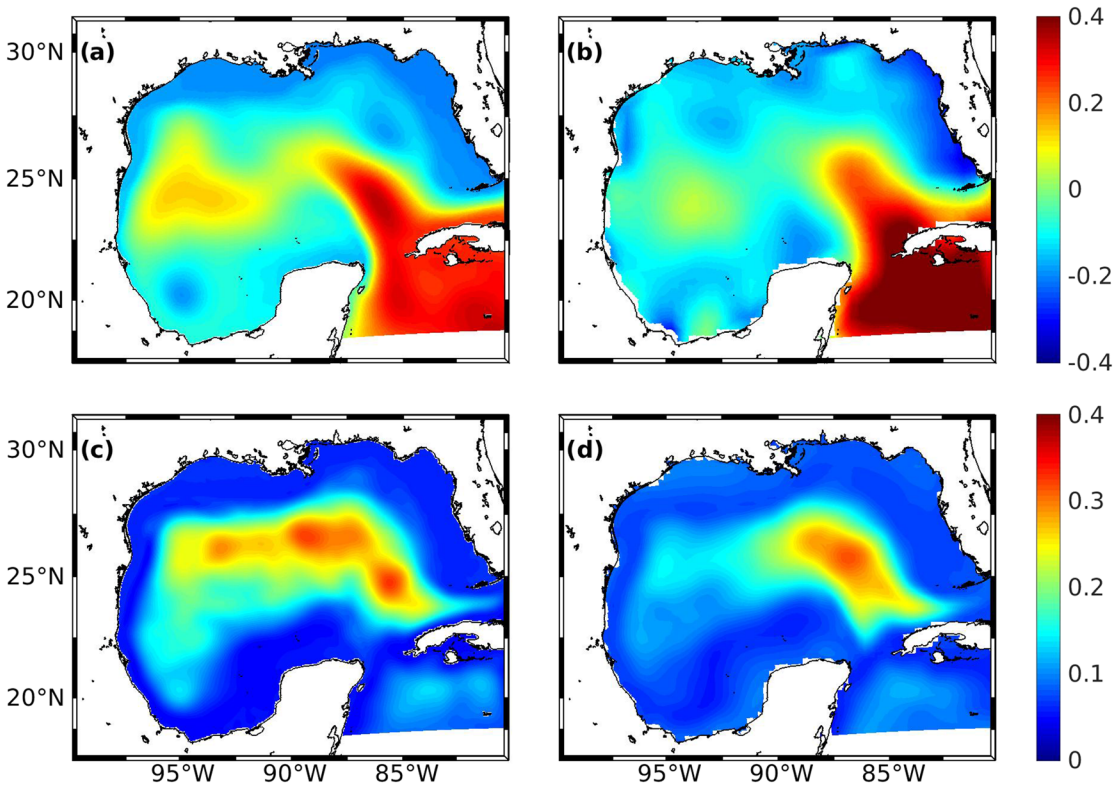

Figure 5. (a) Model-derived mean surface height (m), (b) altimeter-derived mean dynamic topography (m), and (c) model- and (d) altimeter-derived standard deviation of high-frequency sea level anomaly (m).

Mississippi-Alabama continental shelves (Figures 5c and 5d). High variability of the high-frequency SLA west of the Loop Current is a result of the Loop Current warm-core rings or eddies, which dominate the dynamics in the western GoM (e.g., Cardona & Bracco, 2016). Mesoscale variability west of the Loop Current is stronger in the model compared to altimeter observations, consistent with previous modeling studies (e.g., Cardona & Bracco, 2016; Xue et al., 2013). This is likely due to the presence of eddies at a scale comparable to or smaller than the resolution of the SLA maps. In this region, the first baroclinic Rossby deformation radius is around 20 km (Chelton et al., 1998), smaller than the resolution of the gridded altimeter-derived SLA maps, while in the region of the Loop Current, the scale of the Loop Current is well-resolved by the satellite altimeters.

The overall agreement between the model and the observation over the GoM from multiple sources justifies the choice of model parameters, model configuration, and lateral and surface boundary conditions.

4. Wave Climate in the GoM

In this section, we explore the seasonal climatology of significant wave height and its interannual variability.

4.1. Climatology of Significant Wave Height

Significant wave height displays a strong seasonal cycle over the GoM (Figures 6a–6d). Mean H_s is the largest during winter (DJF) (Figure 6a) and is the smallest during summer (JJA) (Figure 6c) over the majority of the GoM. The seasonality of mean H_s generally follows that of U_{10} (Figure 2). The westward direction of the wind over the GoM causes an evident zonal gradient in mean H_s: the mean H_s values are generally the largest in the western part of the GoM, reaching as much as 1.8 m in winter (Figure 6a). Mean H_s is generally small in the Bay of Campeche, the west Florida slope, and the WFS due to the limited fetch. For instance, the mean H_s drops below 0.5 m in the WFS during summer (Figure 6c). Over the majority of the GoM, waves travel westward. Waves are directed southwestward in the Bay of Campeche in all seasons (Figures 6a–6d) and northwestward in the WFS in spring and summer (Figures 6b–6c).

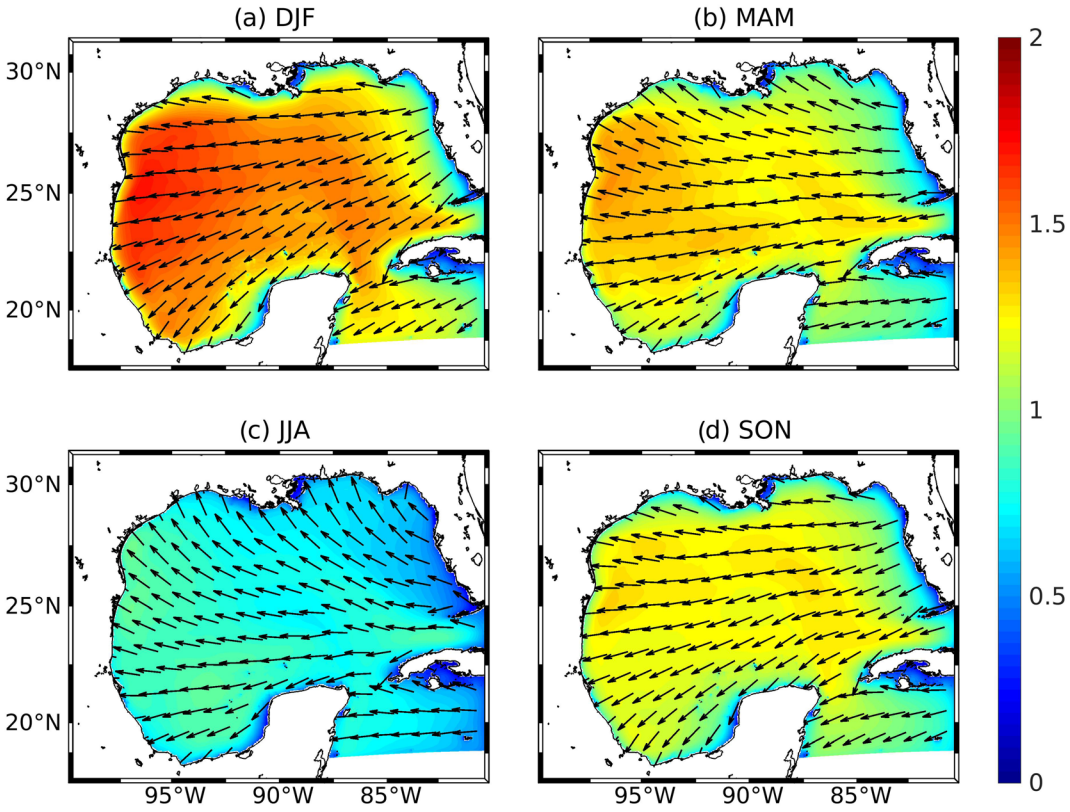

Figure 6. Seasonal climatology of H_s (m) (color) and wave direction (arrows) in the coupled simulation for (a) DJF, (b) MAM, (c) JJA, and (d) SON.

4.2. Interannual Variability of Significant Wave Height

Existing studies have demonstrated the influence of extreme atmospheric phenomena, such as storms, on waves (e.g., Hope et al., 2013). Storms likely play a role in the interannual variability of waves. To examine the interannual variability of wave dynamics and how it is affected by the storms, time series of monthly and spatially averaged H_s anomalies are calculated in four regions (namely, northeastern, southeastern, northwestern, and southwestern GoM) using the point with coordinates of 25°N 91°W (shown with "*" in Figure 1). Dividing the GoM into these regions allows for better identification of local and nonlocal effects of hurricanes on waves. The anomaly is obtained by removing the mean and seasonal cycle from the time series. The strongest positive H_s anomalies are all associated with major hurricanes in the GoM. For instance, clear peaks in H_s anomaly in the southeastern GoM occur during Hurricanes Ivan (2004), Wilma (2005), Ike (2008), and Gustav (2008) (Figure 7b), all of which had traveled through that region (Figure 7a). Intense winds associated with hurricanes drive high waves along their paths and increase H_s considerably (Figure S4a). There are several positive anomalies not associated with hurricanes occur during the colder months. Those large positive anomalies are likely due to cold fronts that are common in the GoM (e.g., Appendini et al., 2018). The distinct negative anomalies, however, generally correspond to the negative anomalies in the wind intensity (e.g., months of September of 2006 and 2009 over the entire GoM). The interannual variability of wave height in the GoM is strongly tied to that of the wind and is influenced by the hurricanes, even though the long-term wind products underestimate the actual hurricane wind intensity (Hodges et al., 2017).

5. Effects of the Loop Current and Eddies on Waves

Currents affect wave heights primarily via four mechanisms. First, analogues to deep-water waves moving into shallow water, when waves travel over an opposing current, the wave energy propagation speed decreases, and the convergence of wave action density increases the wave height due to shoaling, and vice

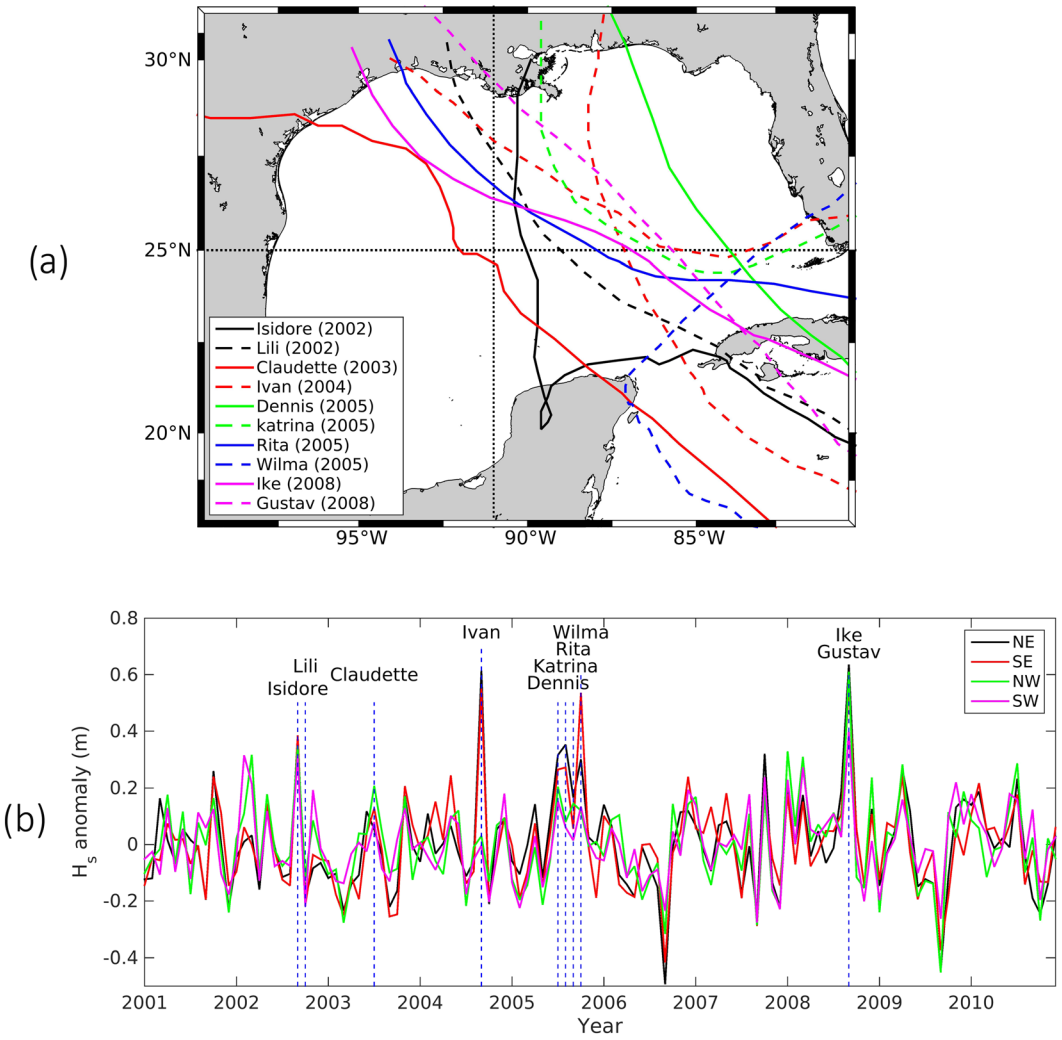

Figure 7. (a) Track of major hurricanes during 2001–2010 in the Gulf of Mexico. The dotted lines indicate how the domain is divided into the four regions. Hurricane track data are from NOAA's National Hurricane Center (NHC). (b) Time series of monthly and spatially averaged H_s anomaly (NE = northeastern GoM; SE = southeastern GoM; NW = northwestern GoM; and SW = southwestern GoM). The dashed lines indicate the months during which the hurricanes impacted the GoM. Marks on the x axis indicate January of the year. Hurricane data are from NOAA's National Hurricane Center (NHC).

versa (Booij et al., 1999). Second, the opposite direction of currents and the wind increases the relative wind speed (Equation 8) and the wind energy input to the waves, leading to larger amplitude waves, and vice versa. Furthermore, wave refraction by spatially variable current fields converges and diverges the wave energy, also altering the wave height both where the current shear is present and where the waves travel to. Ardhuin et al. (2017) found that refraction is the dominant effect for large- and meso-scale ocean currents at scales larger than 50 km, and is overtaken by advective effects for meso to submesoscale currents with scales smaller than 50 km. Finally, the aforementioned mechanisms alter the wave energy carried by swell from its generation area, causing changes in the wave heights in the regions that swells travel to.

5.1. Shoaling and Relative Wind Speed

This section focuses mainly on the local effects of the Loop Current and mesoscale eddies on H_s, which include the current-induced shoaling and the relative wind speed effects. Two snapshots of H_s in the coupled simulation and H_s difference between the coupled and the SWAN-only simulations are shown in Figure 8. The current field, wave direction, and wind direction vectors are also shown in the background of Figure 8.

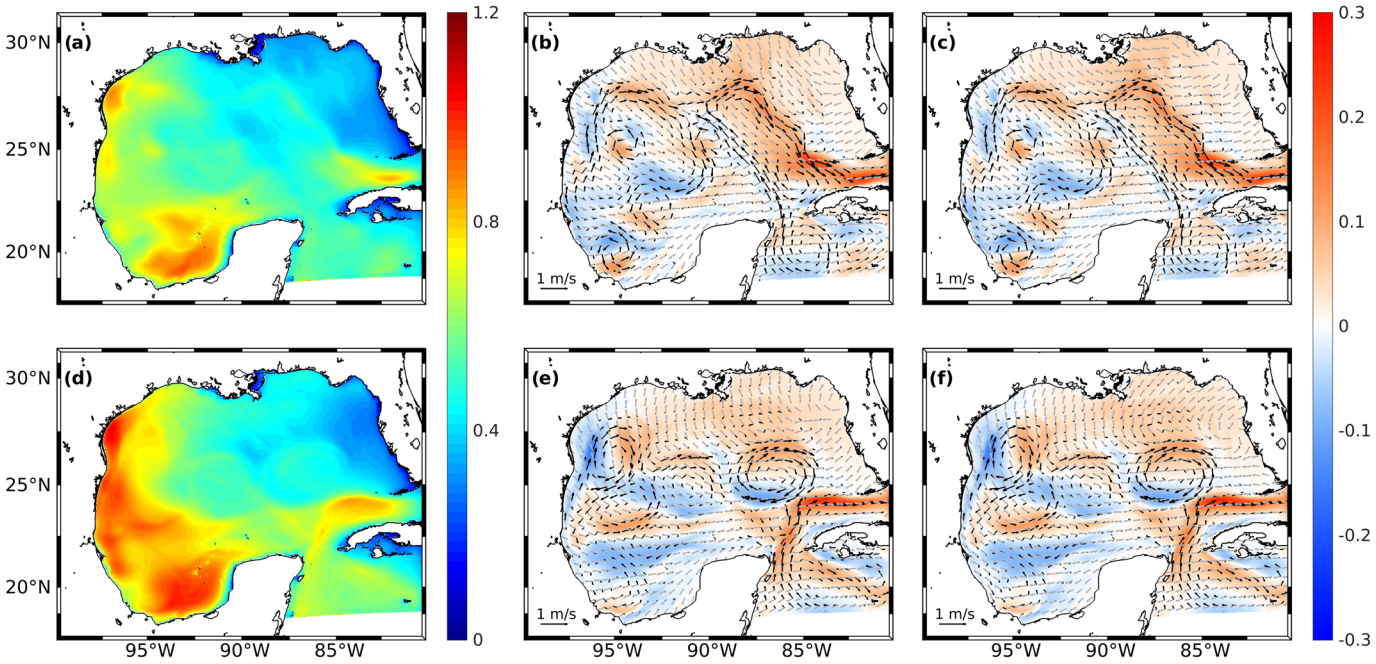

Figure 8. (a) H_s (m) in the coupled simulation, (b) difference in H_s (m) between the coupled and the SWAN-only simulations (color), surface currents direction and magnitude (black arrows) and wave direction (gray arrows) when the Loop Current extends far north. (c) Same as (b) except that the gray arrows indicate wind direction. Panels (d), (e), and (f) same as (a), (b), and (c), respectively, except for when the Loop Current turns east just north of Cuba.

In the first snapshot (Figures 8a–8c), the Loop Current extends far north into the GoM, close to the Louisiana-Texas and Mississippi-Alabama continental shelves. The largest current-induced increase in H_s, accounting for about 0.3 m (35%) of the total H_s, occurs along the eastern branch of the Loop Current, where the currents oppose both the waves (Figure 8b) and the wind (Figure 8c). H_s is also higher over the northern and eastern areas of the warm-core anticyclonic eddy west of the Loop Current. In these regions, currents have an eastward component, opposing the waves (Figure 8b) and the wind (Figure 8c). The largest current-induced decrease in H_s occurs over the northern part of the cyclonic eddy in the western Bay of Campeche and the southern area of the anticyclonic eddy west of the Loop Current. The decrease is about 0.2 m (25%) of the total H_s. This is due to the waves traveling in the same direction of currents (Figure 8b), as well as the decreased relative wind speed when the currents are in the same direction as the wind (Figure 8c). In the second snapshot (Figures 8d–8f), the Loop Current retreats far to the south and leaves the GoM through the Florida Strait right after entering the GoM. An area of large current-induced increase in H_s is the northern part of the newly detached anticyclonic eddy north of the Loop Current, where currents flow eastward in association with the northern and eastern margin of that anticyclonic eddy. The greatest current-induced decrease in H_s is apparent on the opposite side (western and southern margins) of the same anticyclonic eddy and on the western part of an anticyclonic eddy in the northwestern GoM. Examining the overall distribution of H_s difference and the relative intensity of currents indicates that the effects of shoaling and relative wind speed are dominant when the currents are strong.

5.2. Refraction

Refraction not only has a local effect on waves but also can have a stronger nonlocal effect. This is because it can influence the regions that the refracted waves travel to more than the region that actually causes the refraction (e.g., Rapizo et al., 2014). Additionally, because the intensity of refraction is associated with the intensity of the current shear, and not the current itself, it can dominate areas other than those with the strongest currents. To have a better understanding of the effect of refraction on H_s differences shown in Figure 8, ray tracing analysis is used to demonstrate how the waves are refracted by the strongly sheared currents in the GoM, including the Loop Current and the eddies. The ray equations are (e.g., Liu et al., 1989)

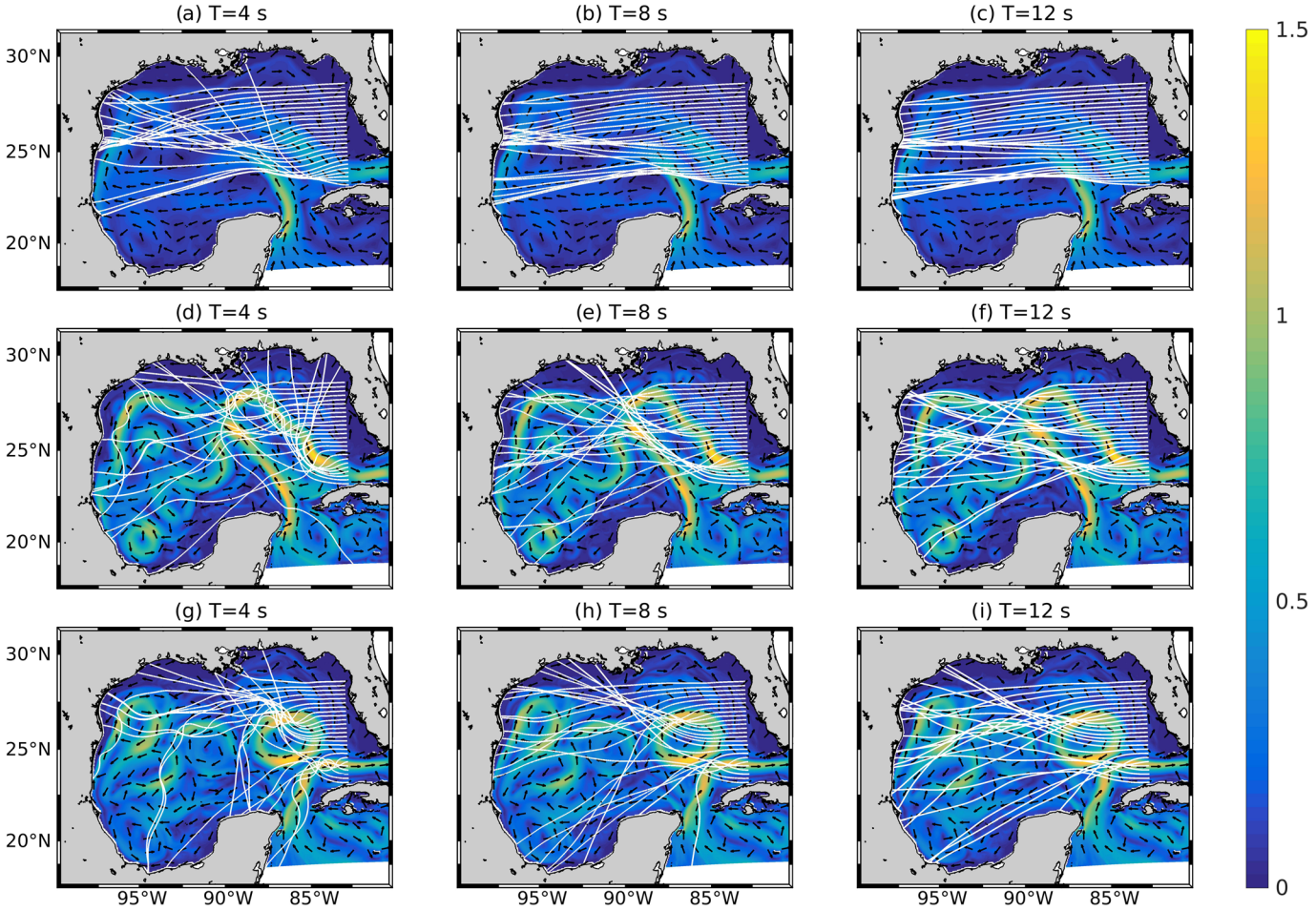

Figure 9. The paths of initially westward wave rays originating from approximately 83°W for (a)–(c) mean state of the GoM currents, (d)–(f) when the Loop Current extends far north, and (g)–(i) when the Loop Current turns east just north of Cuba. Panels on the left correspond to $T = 4$ s, middle panels correspond to $T = 8$ s, and panels on the right correspond to $T = 12$ s. Colors and black arrows show the surface current speed (m/s) and direction, respectively.

$$\frac{d\vec{r}}{dt} = \vec{U}_c + \vec{C}_g \tag{10a}$$

and

$$\frac{d\vec{K}}{dt} = -\vec{K}.\nabla\vec{U}_c, \tag{10b}$$

where $\vec{r} = (x, y)$ is the location of the wave ray, $\vec{C}_g = \left(C_{gx}, C_{gy}\right)$ is the wave group velocity vector, and $\vec{K} = \left(K_x, K_y\right)$ is the wavenumber vector. The absolute frequency is $\omega = \sigma + \vec{K} \cdot \vec{U}_c$, where the intrinsic frequency is determined by the deep-water dispersion relationship as $\sigma^2 = g\left|\vec{K}\right|$. Both current shear and bottom topography induce gradient in wave propagation speed and refraction. Since we are primarily looking at the refraction in the open ocean, the effect of bottom topography, which may have an important effect on wave refraction in coastal ocean (e.g., Kukulka et al., 2017), is neglected. The same equations have been used to examine wave refraction by different currents, including the Gulf Stream meanders (Wang et al., 1994), circulation in the Gulf of Alaska (Liu et al., 1994), and submesoscale frontal currents, off California and the currents at the Loop Current edge in the Northern GoM, off the Alabama coast (Romero et al., 2017).

The ray equations are integrated with three different GoM current fields. The first current field is the climatological mean currents (Figures 9a–9c). In the second (Figures 9d–9f) and third (Figures 9g–9i) scenarios,

the current fields are the same as those in the snapshots in Figures 8a and 8d, respectively, and are intended to illustrate the effects of mesoscale circulations in the GoM, such as eddies, in addition to the Loop Current. The ray tracing experiments are performed for wave rays of three representative wave periods, namely, $T = 4$, 8, and 12 s. Wave rays of the first two periods ($T = 4$ and 8 s) represent wind sea, and wave rays of $T = 12$ s represent swell. All rays originate from the eastern GoM and have an initial westward propagation direction, consistent with the dominant westward wave direction in the GoM (Figure 6). Since rays have a westward component ($K_x < 0$), it is the sign of the meridional shear of the zonal current that determines the northward/southward refraction of the rays: if the zonal current has a positive meridional gradient, the rays are refracted northward and vice versa (Equation 10b). In the case with the climatological currents (Figures 9a–9c), wave rays that originate between ~24°N and 26°N are first refracted southward by the eastern branch of the Loop Current and then northward by the western branch of the Loop Current. The rays emanating north of ~26°N are only able to travel through the anticyclonic circulation associated with the retroflection of the Loop Current and are refracted southward. This leads to the convergence of rays in the northwestern GoM. Refraction decreases with increasing wave period. The refraction pattern is more complex when the instantaneous current fields including high-frequency variabilities, such as eddies, are used. In the first instantaneous current field, the Loop Current extends close to the Louisiana-Texas and Mississippi-Alabama continental shelves (Figures 9d–9f). Refraction by the Loop Current is stronger than that shown in Figures 9a–9c because the instantaneous Loop Current is stronger and narrower than its mean state. Rays from the south of the Loop Current (~23°N) are refracted to their right (northward) toward the northern GoM coast. The origin of these rays is where the wind and the waves oppose the currents, which increases the wind-generated energy (Figure S5a), and part of the additional wave energy is transported to the northern GoM. This can lead to nonlocal increase in wave height in the northern GoM, where the current is weak and is not preferentially opposing the waves and the wind. Some rays of $T = 4$ s even reach the northern WFS. On the other hand, rays from right north of the Loop Current (~28°N) are refracted southward due to the negative meridional shear of the zonal current and reach the Bay of Campeche. The northward refraction of waves that originate from North of Cuba and southward refraction of those from right north of the Loop Current and their subsequent convergence can explain the greater H_s in regions between the northward and southward branches of the Loop Current (Figures 8b–8c), where neither the wind nor the waves oppose the currents. In the snapshot in which the Loop Current turns right north of Cuba into the Florida Strait (Figures 9g–9i), only the paths of rays originating south of ~24°N are affected by the Loop Current. Rays from ~24–28°N, even the fast-traveling swells of $T = 12$ s, are strongly refracted by the newly detached anticyclonic eddy north of the Loop Current (Figure 9i). The rays traveling through the northern and the southern edges of the anticyclonic eddy are refracted to their left (southward) because of the negative meridional shear of zonal current from the radius of maximum velocity toward the eddy boundary. The rays traveling through the core of the eddy are refracted to their right (northward) because of the positive meridional shear of zonal current from the center of the eddy toward the radius of maximum velocity. This is consistent with a previous study on wave refraction by eddies (Mathiesen, 1987). The two anticyclonic eddies in the central and northwestern GoM have a similar but weaker effect on rays compared to the anticyclonic eddy north of the Loop Current because of their weaker current shear. The cyclonic eddies in the western and southwestern GoM refract the rays to their left (southward) when the rays travel through their core and to their right (northward) when the rays travel through their northern and southern edges. Sensitivity experiments with initial ray propagation directions 10°N/S of west show the same qualitative effects of the Loop Current and eddies on the path of the wave rays (Figures S6 and S7).

5.3. The Loop Current Variability and Wave Height Modulation

To assess the influence of Loop Current variability, in terms of its extension into the GoM, on wave heights, the monthly and spatially averaged relative H_s modulation ($\Delta H_s/H_{s,c}$) is calculated over five regions: the eastern and western flanks of the Loop Current, the northeastern coastal GoM, the west central GoM, and the southwestern GoM (Figure 10a). Here ΔH_s is ($H_{s,c} - H_{s,s}$) where $H_{s,c}$ and $H_{s,s}$ are the H_s from the coupled and SWAN-only simulations, respectively. We look at when the Loop Current extends to the north of 28°N (denoted by "N" in Figure 10), and when an eddy detaches and subsequently the Loop Current retreats to the south (denoted by "S" in Figure 10). A total of five Loop Current extension events and eight Loop Current retreat events are identified. The variations in the relative H_s modulation in the eastern flank of the Loop Current are strongly tied to the state of the Loop Current with evident peaks when the Loop

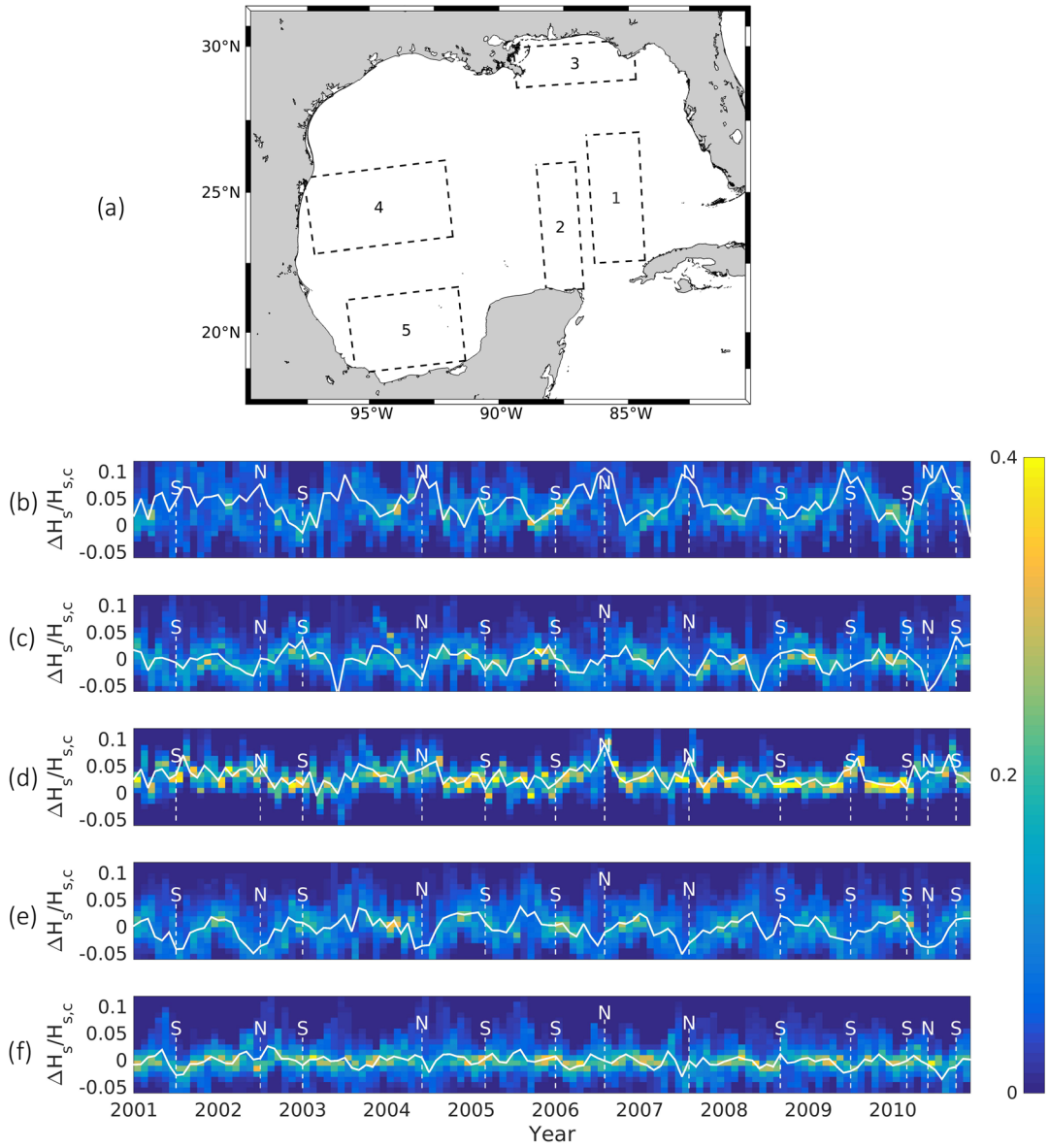

Figure 10. Relative H_s modulation in the five regions shown in (a). Panels (b) to (f) correspond to regions 1 to 5, respectively. "N" and "S" denote northward extension of the Loop Current and eddy shedding events, respectively. Colors show the PDF of relative H_s modulation. Marks on the x axis indicate January of the year.

Current extends northward (Figure 10b). This is consistent with the greater H_s in the coupled simulation over the eastern flank of the Loop Current, mostly due to the shoaling and relative wind effects, as shown in Figures 8a–8c. Modulation is generally negative during eddy shedding events. Also consistent with Figures 8a–8c, the relative H_s modulation in the western flank of the Loop Current is generally negative when the Loop Current extends to the north (Figure 10c). Over the northeastern GoM coasts, relative H_s modulation is positive when the Loop Current extends northward (Figure 10d), which is due to the northward refraction and, therefore, the convergence of the wave rays (Figures 9d–9f). In the west central GoM, modulation is generally negative when the Loop Current extends northward (Figure 10e). This can be due to the presence of following currents associated with the southern parts of the anticyclonic eddies. The modulation over the southwestern GoM is less pronounced than the other four regions and does not appear to be strongly tied to the state of the Loop Current (Figure 10f). The probability density functions (PDFs) of relatively small current effect are highest over the northeastern GoM coasts and the Bay of Campeche, respectively (Figures 10d and 10f), likely due to weaker currents and the lack of organized

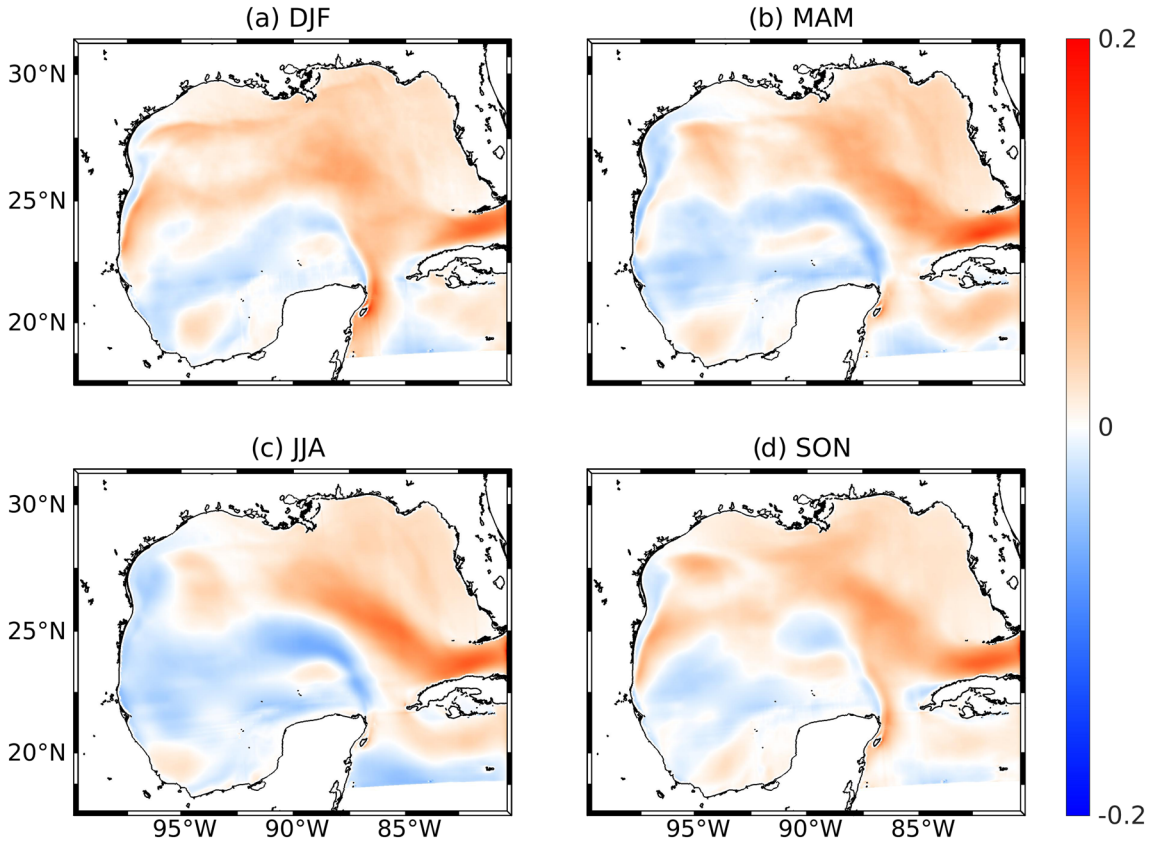

Figure 11. Seasonal climatology of difference in H_s (m) between the coupled and the SWAN-only simulations for (a) DJF, (b) MAM, (c) JJA, and (d) SON.

current systems in the region compared to that in the eastern and western flanks of the Loop Current (Figures 10b–10c). The PDFs of relative modulation of H_s are most spread-out, cover a wider range of values, and are skewed toward the positive values in the eastern flank of the Loop Current (Figure 10b) compared to those in the northeastern GoM, west central GoM, and the Bay of Campeche (Figures 10d–10f). The PDF plots show how the peak in the probability density moves as the location of the Loop Current changes over the study period. For instance, as the Loop Current extends northward, the distribution of relative H_s modulation frequency over the eastern flank of the Loop Current moves toward the positive values, following the line of mean modulation (Figure 10b).

5.4. Long-Term and Short-Term Wave Height Modulation

In this subsection, we focus on both long-term and short-term effects of currents on waves. The long-term effects are examined by looking at the seasonal climatology of H_s difference between the coupled and the SWAN-only simulations. While the largest current-induced change in H_s in the snapshots is more than 0.25 m (Figure 8), the mean H_s in the GoM can increase by about 0.18 m and decrease by about 0.15 m at different locations in the GoM in the presence of currents (Figures 11a–11d). The largest positive differences occur at the eastern flank of the Loop Current, where it flows toward the Florida Strait and is in the opposite direction of both the waves and the wind. While the currents do not preferentially oppose or follow the waves or the wind in the WFS (Figure 8), they have a positive effect on the mean H_s difference, implying the transport of swell energy from regions with increased wave energy as well as the convergence of the wave energy due to refraction (Figure 9d). The mean H_s values are generally higher in the coupled simulation south of the Louisiana-Texas and Mississippi-Alabama continental shelves, which can be due to the refraction of wave rays from the south (Figure 9). The regions west of the Loop Current are mostly affected by the anticyclonic eddies detached from the Loop Current. After detaching from the Loop Current, the anticyclonic eddies travel in a mean west-southwestward path in the central GoM basin (e.g., Hamilton et al., 1999;

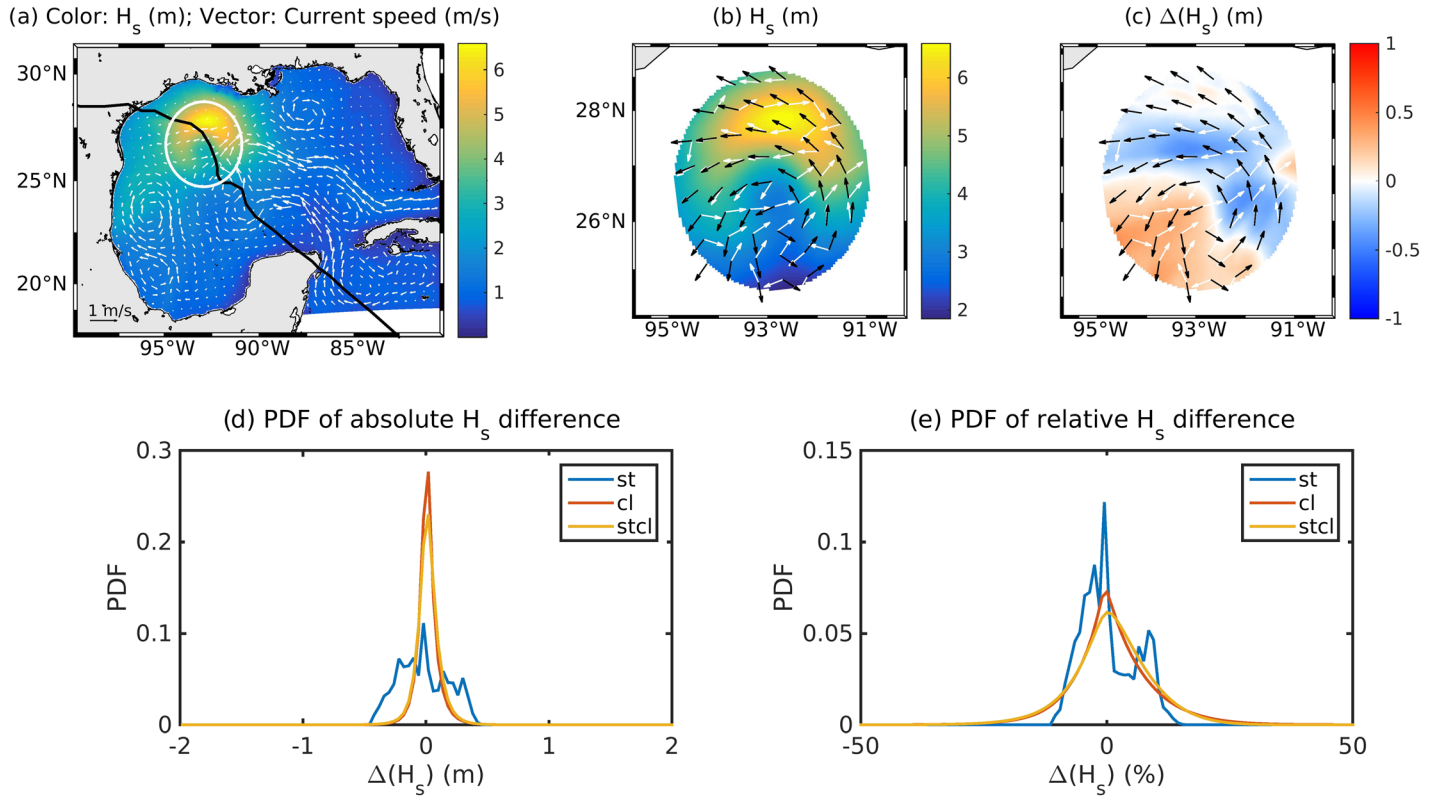

Figure 12. Snapshot of Hurricane Claudette (2003). (a) Color map shows H_S (m) in the coupled simulation. White arrows indicate current direction and speed (m/s). Storm track is shown with the black line. (b) Color map shows H_S (m) in the coupled simulation. Black arrows show wave direction. White arrows show current direction. (c) Difference in H_S (m) between the coupled and SWAN-only simulations (ΔH_S). Vectors are same as those in panel (b). (d) PDFs of absolute instantaneous ΔH_S (m) over the storm region shown by "st," climatological absolute ΔH_S (m) over the storm region shown by "stcl," climatological absolute ΔH_S (m) over the entire GoM shown by "cl." (e) Same as (d) but for $\Delta H_S/H_{S,c}$ (%). In this snapshot, maximum reanalysis and observed wind speeds are $V_{r,max} = 20.2$ m/s and $V_{o,max} = 24.6$ m/s, respectively.

Weisberg & Liu, 2017) and also seen in our results (Figure 5). This causes the wind and the waves, which are mainly directed westward (Figures 2 and 6), to be opposing (following) the currents in the northern (southern) section of the anticyclonic eddies in the western GoM, which increases (decreases) H_s southeast of the LATEX Shelf (northern Bay of Campeche) in the presence of currents. The convergence of wave rays in the northwestern GoM (Figures 9a–9c) can also contribute to greater H_s, whereas the shadow zone in the western GoM between ~22°N and 25°N (Figures 9a–9c) can contribute to smaller H_s in the presence of currents (Figures 11a–11d). The positive (negative) H_s difference in regions in southern (northern) Bay of Campeche can also be a result of the wind and the waves opposing (following) the currents associated with the cyclonic eddies in Figure 8 that frequently occur in the Bay of Campeche (De La Cerda et al., 2005). In total, the mean H_s is modulated by currents by as much as 0.18 m (±15%). There is no evident seasonality in the H_s difference, while H_s displays a strong seasonal cycle probably because the seasonal variability in the strength of the Loop Current is not as significant (Rousset & Beal, 2011) as that of the wind speed and H_s.

Since waves in the GoM are subject to episodic, transient, and extreme meteorological forcing under hurricanes, the effect of currents during hurricanes is also examined and is compared with that under nonhurricane conditions. For this purpose, significant wave height (H_s), the current-induced difference in H_s, and the PDFs of absolute and relative H_s difference for the hurricanes shown in Figure 7 are examined. As mentioned in section 4.2, the reanalysis maximum storm winds ($V_{r,max}$) are weaker than the observed maximum wind ($V_{o,max}$). However, the CFSR wind product that is used in this study provides a better storm wind than many other reanalysis data sets (Hodges et al., 2017). For Hurricane Claudette (2003), H_s is the largest at the

front-right quadrant of the storm (Figures 12a and 12b), consistent with existing numerical (e.g., Chen et al., 2013; Fan et al., 2009) and observational studies (e.g., Walsh et al., 2002; Wright et al., 2001). H_s is mostly smaller in the coupled simulation than in the SWAN-only simulation at the right-hand side of the storm (Figures 12c). This is due to the alignment between the currents and the waves. At the left-hand side of the storm, particularly the rear-left quadrant, currents increase H_s primarily because waves and currents are in the opposing directions. Within a radius of 2° from the center of the hurricane, areas that show negative current-induced effects on H_s are larger than those with positive effects, causing the distribution to be skewed toward the negative values (blue lines in Figures 12d and 12e). The absolute current effect is larger under the hurricane (blue line in Figure 12d) than under nonhurricane conditions both for over the snapshot area (yellow line in Figure 12d) and for over the entire GoM (red line in Figure 12d), as indicated by wider distribution functions. Under the extreme wind of a hurricane, waves are strongly forced, the relative effect of current is, therefore, smaller, implied by a boarder distribution under nonhurricane conditions (Figure 12e) (compare the blue line and the yellow line in Figure 12e). Sensitivity analysis with regards to the distance from the eye of the storms indicated negligible effects of distance on the calculated PDFs.

The different locations of a hurricane relative to the Loop current lead to different qualitative and quantitative effects of currents. For example, responses relatively similar to those of Hurricane Claudette (2003) are seen for Hurricanes Isidore (2002) (Figure S8) and Dennis (2005) (Figure S9), which do not interact with the Loop Current at the snapshot shown in the figures. On the other hand, for Hurricanes Ivan (2004) (Figure S10), Katrina (2005) (Figure S11), Rita (2005) (Figure S12), and Ike (2008) (Figure S13), H_s is greater in the coupled simulation than in the SWAN-only simulation in the frontside of the storm, most likely due to the dominant effects of the Loop Current. This is because the prominent strong westward wind opposes the currents in the northern parts of the Loop Current, which are mostly eastward. Therefore, PDFs of absolute and relative H_s modulation are generally skewed toward positive values. For Hurricane Gustav (2008) (Figure S14), H_s is greater in the coupled simulation than in the SWAN-only simulation in the rear side of the storm due to the interaction with the northern parts of the Loop Current and smaller in the frontside due to the alignment of waves and currents. Interestingly, the interaction of Hurricane Wilma (2008) (Figure S15) with the southward and eastward parts of the Loop Current considerably decreases H_s in the coupled simulation due to the following direction of waves and currents. Since Hurricane Lili (2002) (Figure S16) at this snapshot is located over a highly spatially variable current field inside the Loop Current, currents result in a more symmetric distribution of H_s modulation around zero. These results show that strong currents associated with the Loop Current and their direction can be dominant in storm conditions and lead to increased wave heights in the coupled simulation.

6. Wave Effect on the Atmosphere and the Ocean

Waves mediate the interaction between the ocean and the atmosphere. In this section, we assess the significance of the role that waves play in the two sides of the ocean-atmosphere interface in the GoM by examining parameters including swell fraction, wave age (W_{age}), Stokes drift (u_{st}), and Langmuir number (La).

6.1. Swell

Swells are the nonlocal wave component and play an important role in the ocean-atmosphere momentum flux because they travel faster than wind seas (e.g., Grachev & Fairall, 2001). Although their amplitude is not generally large, swells typically carry a considerable fraction of the wave energy over large distances (Fan et al., 2014) given that their energy decay scales can exceed 20,000 km (Ardhuin et al., 2009).

6.1.1. Climatology of Swell Fraction

The swell fraction of the wave energy over the GoM displays a distinct spatial and temporal variability (Figures 13a–13d). Mean swell fraction is the largest during summer (Figure 13c) and is the smallest during winter (Figure 13a). It is as high as 0.8 almost all year round in the southwestern GoM right off the coast of Mexico, mainly due to the dominant westward direction of the wind and the waves (Figures 2 and 6). The exception of the westward increase in the mean swell fraction is the northeastern GoM during summer (Figure 13c) with mean swell fraction larger than 0.5, which is due to the weak wind ($U_{10} < 4$ m/s) in that region during summer. The average fraction of the swell energy in the wave energy spectrum over the GoM is larger than 0.3.

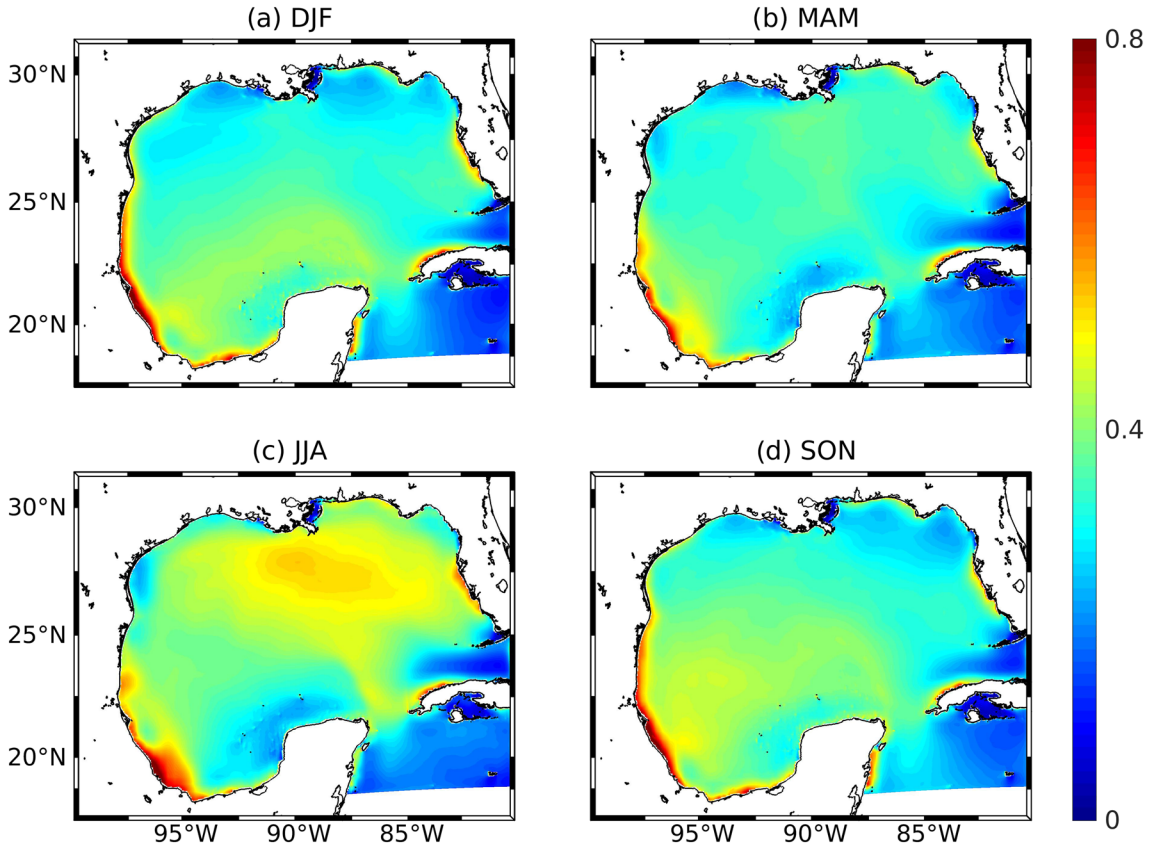

Figure 13. Seasonal climatology of swell fraction in the coupled simulation for (a) DJF, (b) MAM, (c) JJA, and (d) SON.

6.1.2. Interannual Variability of Swell Fraction

Similar to that for H_s (Figure 7), the time series of monthly and spatially averaged swell fraction anomaly is calculated. There are strong positive swell fraction anomalies associated with a number of major hurricanes in areas far from their paths. This is because the strong waves driven by the hurricanes travel across the GoM and result in an increased swell fraction in areas away from the hurricane track (Figure S4b). For instance, Hurricane Ivan (2004) impacted the eastern GoM, while its effect on swell fraction anomaly is most evident in the southwestern GoM (Figure 14). There are also strong positive swell anomalies not associated with any storm, implying that other atmospheric variabilities may contribute to the variability in swell fraction. For example, the swell anomaly is relatively large in the northeastern GoM during April 2002. Analysis of the wind fields of the same period shows that the anomaly is the combined consequence of two phenomena: first, the abnormally weak wind over the region, which makes the wind seas to be less dominant, and second, the southerly wind from the southeastern GoM and the westerly wind from the northwestern GoM, which create a developed sea with higher swell fraction and less coupling to the local wind in the northeastern GoM, compared to when the climatological easterly wind is dominant (Figure 2). These analyses show that swell fraction anomaly is affected not only by the intensity of the wind over a region but also by the wind direction.

6.2. Wave Age

When the inverse wave age ($U_{10}cos\Delta\theta/c_P$) is larger than 0.83, waves are mainly growing by absorbing momentum from the wind, while when the inverse wave age is smaller than 0.15, there are waves fast enough that can transfer momentum back to the air (Hanley et al., 2010). The in-between range, i.e., $0.15 < U_{10}cos\Delta\theta/c_P < 0.83$, indicates a mixed sea state composed of both swells and wind seas. To quantify how often the wave-driven wind regime and the wind-driven wave regime occur in the GoM, the frequencies of occurrence of $U_{10}cos\Delta\theta/c_P < 0.15$ (Figures 15a–15d) and $U_{10}cos\Delta\theta/c_P > 0.83$ (Figures 15e–15h) are

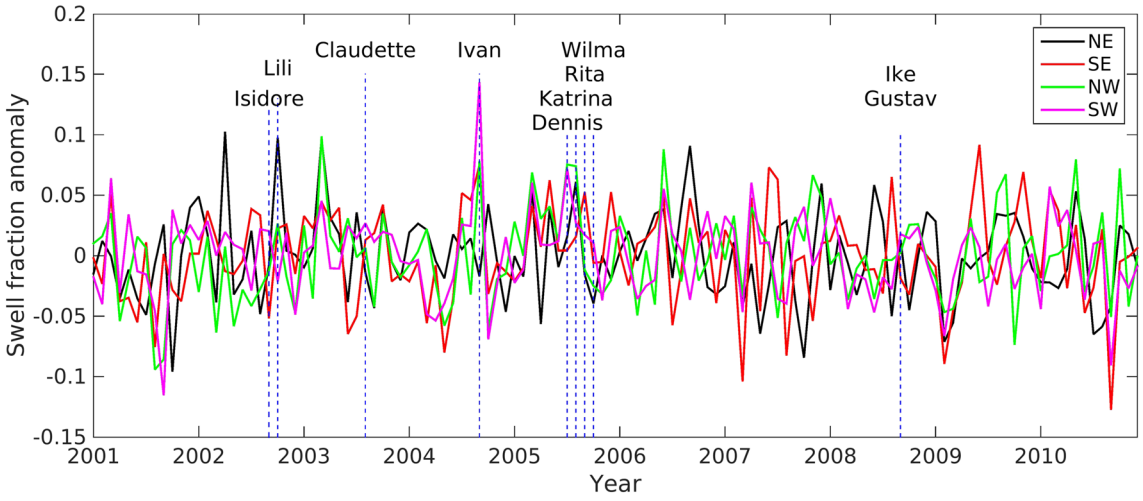

Figure 14. Time series of monthly and spatially averaged swell fraction anomaly. NE, SE, NW, and SW are defined the same as Figure 7. The dashed lines indicate the months during which the hurricanes impacted the GoM. Marks on the *x* axis indicate January of the year. Hurricane data are from NOAA's National Hurricane Center (NHC).

calculated. There is a relatively high frequency (more than 25% of the time) of occurrence of $U_{10}cos\Delta\theta/c_P < 0.15$ during summer over the northeastern GoM (Figure 15c), implying a greater prevalence of the wave-driven wind regime. This region coincides with that exhibiting low U_{10} values (Figure 2c) and high swell fractions (Figure 13c). The wave-driven wind regime is most frequent (more than 70% of the time) and occurs almost consistently in all seasons in the southwestern GoM, off the coast of Mexico. This is mainly because of the presence of fast-traveling swell originating from the east (Figure 13) and the weaker wind (Figure 2). The frequency of occurrence of $U_{10}cos\Delta\theta/c_P < 0.15$ drops below 0.05 over a large part of the GoM during spring, especially south of ~25°N, suggesting that waves are strongly coupled to the wind. Frequency of occurrence of $U_{10}cos\Delta\theta/c_P > 0.83$ shows how frequent the wind-driven wave regime occurs.

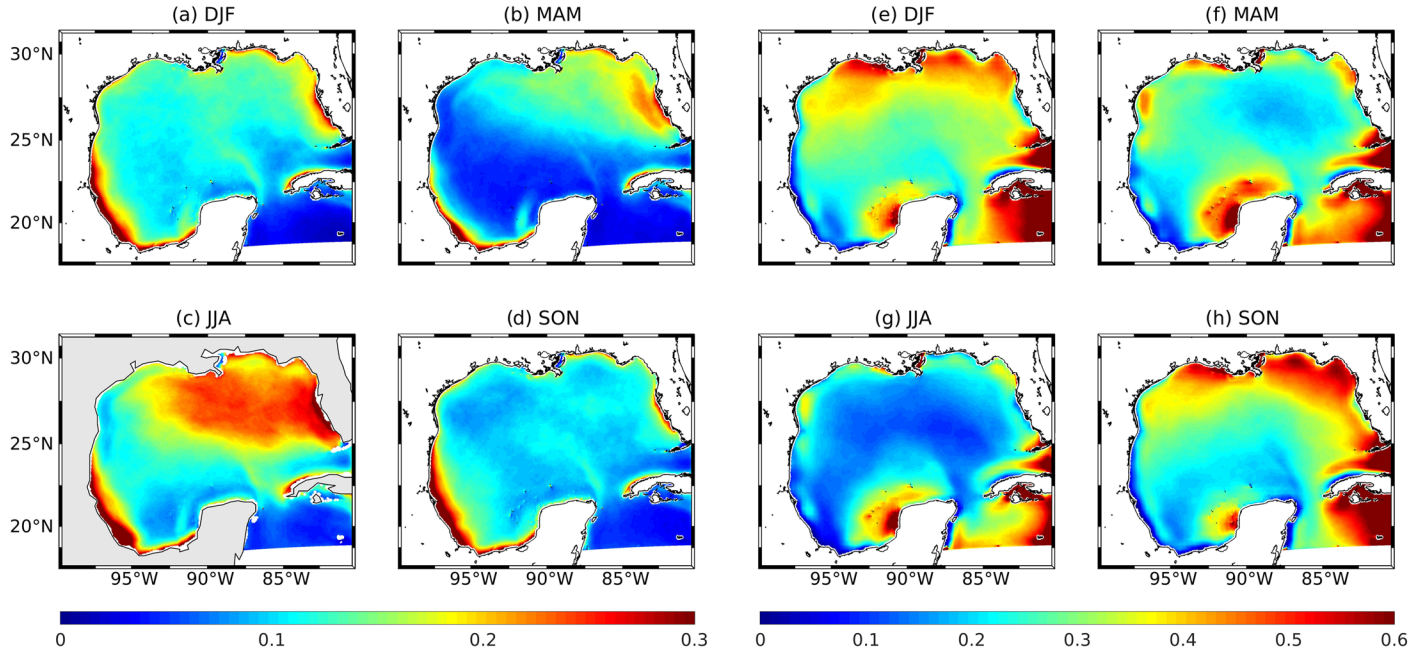

Figure 15. Seasonal climatology of frequency of occurrence of $U_{10}cos\Delta\theta/c_P < 0.15$ in the coupled simulation for (a) DJF, (b) MAM, (c) JJA, and (d) SON, and seasonal climatology of frequency of occurrence of $U_{10}cos\Delta\theta/c_P > 0.83$ in the coupled simulation for (e) DJF, (f) MAM, (g) JJA, and (h) SON.

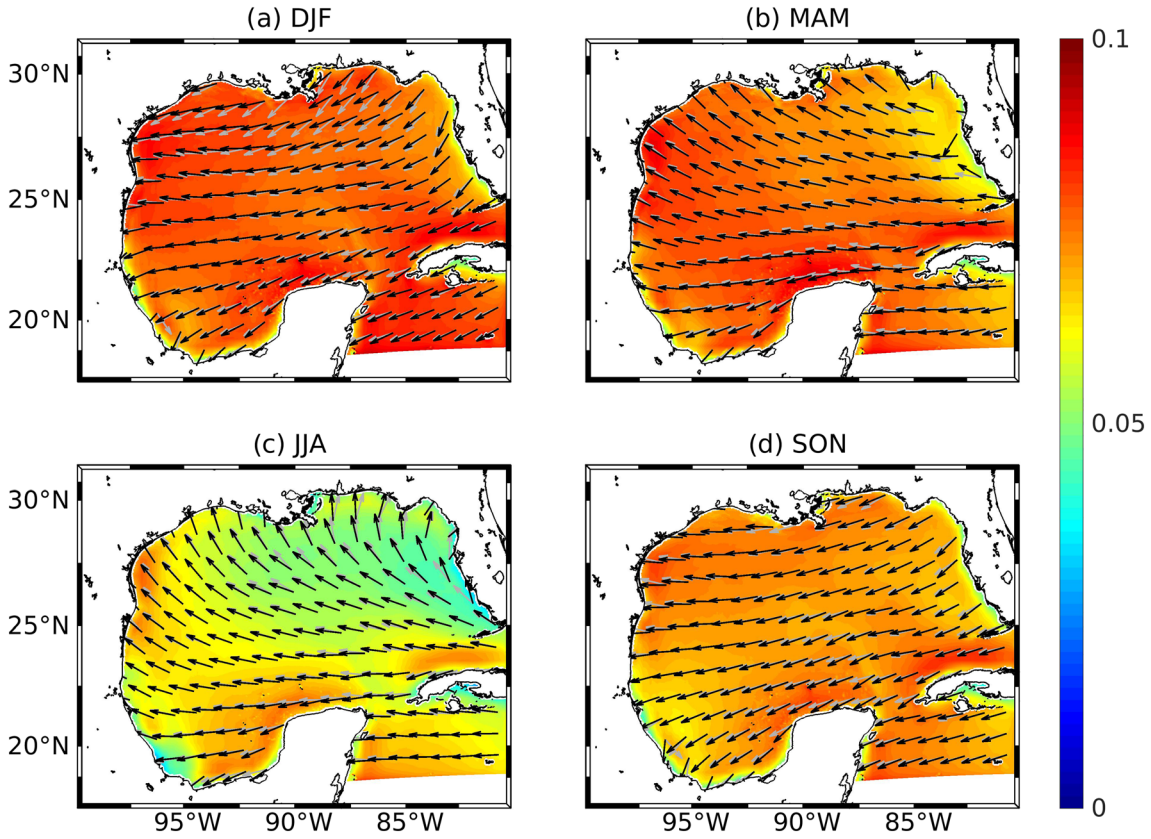

Figure 16. Seasonal climatology of Stokes drift magnitude (m/s) (color) and direction (black arrows) in the coupled simulation and wind direction (gray arrows) for (a) DJF, (b) MAM, (c) JJA, and (d) SON.

Wind-driven wave regime (Figures 15e–15h) is most frequent in the LATEX Shelf and west of the Yucatan Peninsula (more than 60% of the time). The frequency of occurrence of the wind-driven wave regime in fall and winter is greater than in spring and summer and displays a meridional gradient with a stronger coupling of waves to the wind in higher latitudes. The U_{10} maps (Figure 2) display similar meridional variation during those seasons. The wind-driven wave regime is less prevalent during summer (~10% of the time), which is consistent with the weakest wind during summer (Figure 2c). These conclusions are also in line with the maps of inverse wave age climatology (Figure S17).

6.3. Stokes Drift

Stokes drift contributes to the horizontal transport at the ocean surface (e.g., Kenyon, 1969; Weisberg & Liu, 2017). It can play an important role when swell is strong and is in different directions from the currents. Mean Stokes drift is generally greater in the northwestern GoM, the Campeche Bank, north of Cuba compared to other regions in the GoM (Figures 16a–16d). The seasonal variation in the Stokes drift magnitude in the GoM is to some extent similar to that of U_{10} (Figure 2). Mean Stokes drift is the largest and exceeds 0.09 m/s in winter (Figure 16a), when the wind is the strongest (Figure 2a). Mean Stokes drift is the smallest and drops below 0.04 m/s during summer, when the wind is weak ($U_{10} < 4$ m/s), particularly in the west Florida slope, the WFS, and the LATEX Shelf (Figure 16c). Stokes drift ranges from 0.03 to 0.10 m/s in the GoM, which agrees with the calculations by Clarke and Gorder (2018) using observations from buoys in the GoM. Mean Stokes drift is dominantly westward, while it is directed southwestward in the Bay of Campeche and Campeche Bank throughout the year. It is southwestward in the WFS in fall and winter (Figures 16d and 16a), and northwestward in summer and spring (Figures 16b–16c). Stokes drift mostly aligns with the wind, especially in spring and fall (Figures 16b and 16d) with a few regions displaying slight misalignments. In winter, the Stokes drift-wind misalignment is the greatest south of the Louisiana-Texas and Mississippi-Alabama shelves (Figure 16a), where the Stokes drift is directed to the north of the wind.

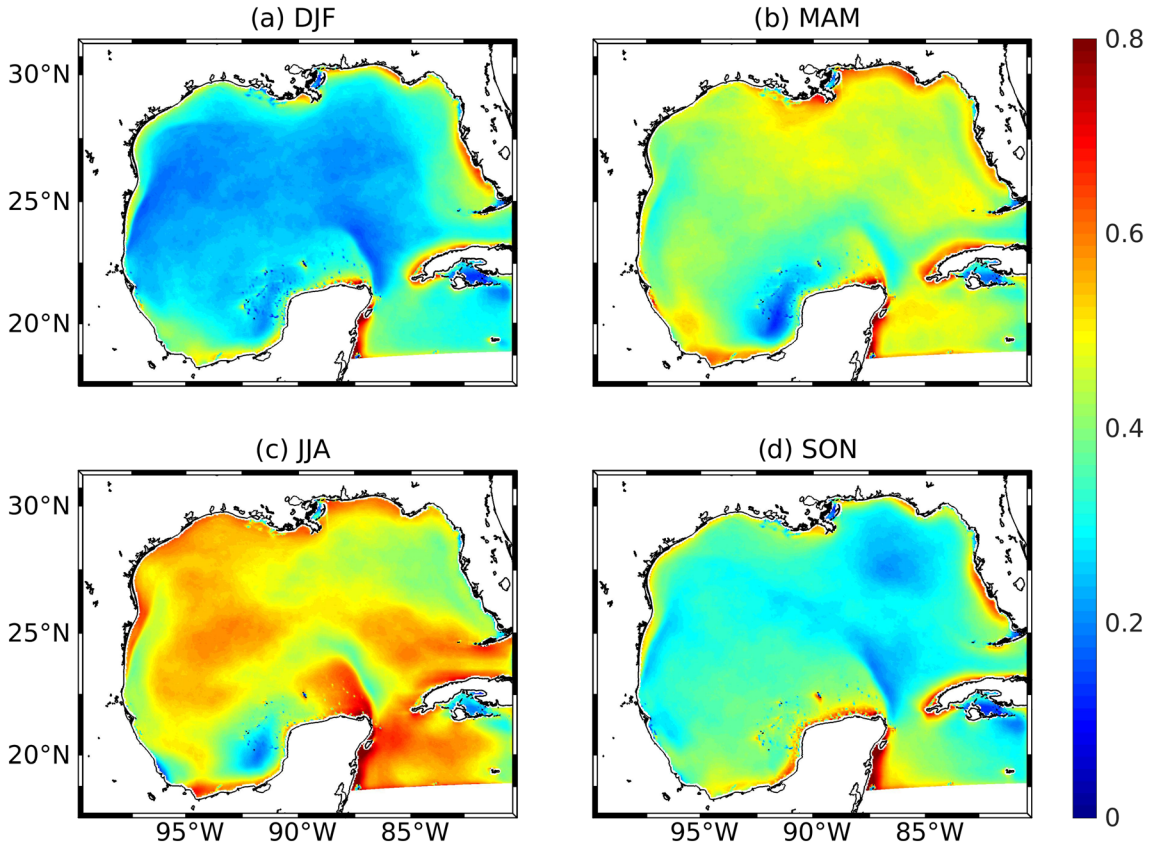

Figure 17. Seasonal climatology of frequency of occurrence of La<0.30 in the coupled simulation for (a) DJF, (b) MAM, (c) JJA, and (d) SON.

Although high-frequency wind seas have a higher contribution to Stokes drift, Stokes drift in summer (Figure 16c) is small enough to be affected by the low-frequency swells in the northeastern GoM (Figure 13c), resulting in the misalignment between Stokes drift and the wind.

6.4. Langmuir Number

The significance of wave-driven Langmuir turbulence is assessed using the turbulent Langmuir number (La) (Equation 2). Belcher et al. (2012) show that more than 90% of the turbulent kinetic energy in the OSBL is from the waves when La<0.3. The frequency of occurrence of La<0.30 (Figures 17a–17d) is therefore examined. The importance of wave-driven Langmuir turbulence is variable spatially and temporally in the GoM. The lowest mean frequency of occurrence of La<0.30 occurs during winter (~0.2), when the strong winds (U_{10} > 8 m/s) occur. In spring, a pool with a relatively high frequency (>0.5) of occurrence of La<0.30 over the northeastern GoM (Figure 17b) coincides with that with low U_{10} (Figure 2b) and implies a greater role for wave-driven turbulence within the OSBL. Low wind speed (Figure 2c) and large swell fraction (Figure 13c) during summer are favorable for the frequency of dominance of wave-driven turbulence to reach as high as 0.6 over the majority of the GoM (Figure 17c), implying the greater contribution of wave forcing.

7. Summary

The GoM is a semienclosed sea with a relatively small amount of swell traveling into it from the Atlantic Ocean and the Caribbean Sea (Fan et al., 2014). This causes the spatial and temporal variability in the surface gravity waves in the GoM to be strongly tied to that of the overlying wind field, especially in the eastern GoM. The exception is summer when the swell fraction exceeds 0.5 south of the LATEX Shelf. The swell fraction is generally larger in the western GoM in all seasons because the prevailing wind is westward, causing the western GoM to be a more developed and swell-dominated sea. The east-west gradient in the swell fraction is

consistent with a previous study using the ERA-40 global data set (Semedo et al., 2011). High swells along the western GoM coasts can contribute to coastal erosion through resuspension and transport of sediments away from the nearshore zones (Smith et al., 2010). Although the GoM is not as vast as the major oceanic basins, such as the Southern Ocean or the Pacific Ocean, and the waves in the GoM have a limited fetch and are driven by weaker wind, our results show that the wave-driven wind regime can still occur frequently in the GoM, especially in the northeastern GoM in summer. Wave-driven turbulence can play an important role in mixing in OSBL in the GoM. The high spatial and temporal variability in frequency of occurrence of $La<0.3$ in the GoM suggests that the wind forcing and the wave forcing are not at a constant ratio in the GoM. This necessitates the explicit inclusion of a parameterization for wave-driven mixing (e.g., Harcourt, 2015; Reichl et al., 2016; Sinha et al., 2015) in the region, which may improve the simulated mixed layer depth and sea surface temperature estimates in ocean models. Our results show that the wave effects on both the ocean and the atmosphere, in terms of air-sea momentum flux and wave-driven mixing, are more pronounced when the wind is weak. While the storm effects on significant wave height are mainly local and seen over the paths of storms, the effect on swell fraction is mostly nonlocal and occurs in areas far from the paths of storms. Results show that waves are significantly affected by the currents in the GoM. It should be noted that although there are uncertainties in the long-term surface current simulation in terms of exact intensity and location of the Loop Current and eddies, the present model provides statistical insights on how these currents affect surface gravity waves in the GoM. This study is the first step toward better understanding and modeling of the coupling among atmosphere, wave, and ocean in the GoM. The coupled modeling of the three components of the earth system has recently been carried out in other regions such as the Gulf Stream (Shi & Bourassa, 2019) and the Baltic Sea (Wu et al., 2019). Those studies demonstrate that the coupling alters the simulated mean states of the three earth system components and the fluxes among them. Similar coupling studies will be carried out for the GoM in future studies.

In summary, the most important conclusions of this study are the following:

1. Ocean currents alter the mean significant wave heights by as much as 0.18 m (±15%) in the GoM, while the current-induced modulation of significant wave heights can reach up to 0.3 m (±35%) during individual low wind snapshots. The modulation can exceed 1 m in storm conditions.
2. The swell fraction of the wave energy generally increases from the east to the west in the GoM and exceeds 0.8 in the southwestern GoM, off the coast of Mexico. Swell fraction is the largest in summer and is the smallest in winter.
3. The GoM is generally in a mixed state in terms of air-sea momentum flux. However, the wave-driven wind regime is prevalent and occurs more than 70% of the time in the southwestern GoM, off the coast of Mexico. The wind-driven wave regime, on the other hand, is most prevalent in the WFS and west of the Yucatan Peninsula.
4. The direction of surface Stokes drift closely follows that of the 10-m wind with slight misalignment in the northeastern GoM, especially in winter and summer.
5. The wave-driven Langmuir turbulence has a greater contribution to the OSBL mixing in the GoM in spring and summer than in fall and winter. The spatial and temporal variability in the frequency of occurrence of $La<0.30$ suggests the variable contributions of wave-driven and wind-driven mixing in the OSBL in the GoM.

Acknowledgments

We thank the two anonymous reviewers for their valuable comments and suggestions that have substantially improved this paper. We acknowledge the use of open source models ROMS and SWAN, and the COAWST modeling framework. The CFSR data set can be accessed at https://rda.ucar.edu/datasets/ds093.1/ (free registration is required). The SODA data set is available at https://www2.atmos.umd.edu/~ocean/index_files/soda3.7.2_mn_download.htm. Mean dynamic topography (MDT) data (MDT_CNES-CLS13) was produced by CLS and distributed by Aviso+, with support from Cnes and is available at ftp://ftp-access.aviso.altimetry.fr/auxiliary/mdt (free registration may be required at https://www.aviso.altimetry.fr/). This study has been conducted using E.U. Copernicus Marine Service Information. The SLA data are available at http://marine.copernicus.eu/services-portfolio/access-to-products/ (SEALEVEL_GLO_PHY_L4_REP_OBSERVATIONS_008_047 data set). Altimeter-derived wave height data are provided by IFREMER and are available at ftp://ftp.ifremer.fr/ifremer/cersat/products/swath/altimeters/waves/data/. Buoy data are provided by NOAA's National Data Buoy Center (NDBC, http://www.ndbc.noaa.gov). Hurricane data are provided by NOAA's National Hurricane Center (NHC, https://www.nhc.noaa.gov/data/). Model solutions are available at https://doi.org/10.5281/zenodo.3526585. EA, JHL, and JL were supported by the National Science Foundation through grants OCE-1521018 and OCE-1558317. YF was funded under the Naval Research Laboratory base program BE031-03-42-1G35. JHL, QC, and JL were supported by National Science Foundation through grant CCF1539567. Computations were performed using high performance computing resources provided by Louisiana State University and by the Louisiana Optical Network Infrastructure.

References

Akpınar, A., & Bingölbali, B. (2016). Long-term variations of wind and wave conditions in the coastal regions of the Black Sea. *Natural Hazards*, *84*(1), 69–92. https://doi.org/10.1007/s11069-016-2407-9

Alvera-Azcárate, A., Barth, A., & Weisberg, R. H. (2009). The surface circulation of the Caribbean Sea and the Gulf of Mexico as inferred from satellite altimetry. *Journal of Physical Oceanography*, *39*(3), 640–657. https://doi.org/10.1175/2008JPO3765.1

Appendini, C. M., Hernández-Lasheras, J., Meza-Padilla, R., & Kurczyn, J. A. (2018). Effect of climate change on wind waves generated by anticyclonic cold front intrusions in the Gulf of Mexico. *Climate Dynamics*, *51*(9-10):3747–3763, https://doi.org/10.1007/s00382-018-4108-4

Appendini, C. M., Torres-Freyermuth, A., Salles, P., López-González, J., & Mendoza, E. T. (2013). Wave climate and trends for the Gulf of Mexico: A 30-yr wave hindcast. *Journal of Climate*, *27*(4), 1619–1632. https://doi.org/10.1175/JCLI-D-13-00206.1

Ardhuin, F., Chapron, B., & Collard, F. (2009). Observation of swell dissipation across oceans. *Geophysical Research Letters*, *36*, L06607. https://doi.org/10.1029/2008GL037030

Ardhuin, F., Chapron, B., & Elfouhaily, T. (2004). Waves and the air–sea momentum budget: Implications for ocean circulation modeling. *Journal of Physical Oceanography*, *34*(7), 1741–1755. https://doi.org/10.1175/1520-0485(2004)034<1741:WATAMB>2.0.CO;2

Ardhuin, F., Gille, S. T., Menemenlis, D., Rocha, C. B., Rascle, N., Chapron, B., et al. (2017). Small-scale open ocean currents have large effects on wind wave heights. *Journal of Geophysical Research: Oceans*, *122*, 4500–4517. https://doi.org/10.1002/2016JC012413

Ardhuin, F., Roland, A., Dumas, F., Bennis, A.-C., Sentchev, A., Forget, P., et al. (2012). Numerical wave modeling in conditions with strong currents: Dissipation, refraction, and relative wind. *Journal of Physical Oceanography*, *42*(12), 2101–2120. https://doi.org/10.1175/JPO-D-11-0220.1

Babanin, A. (2011). *Breaking and dissipation of ocean surface waves* (p. 480). New York, NY: Cambridge University Press. https://doi.org/10.1017/CBO9780511736162

Belcher, S. E., Grant, A. L. M., Hanley, K. E., Fox-Kemper, B., Van Roekel, L., Sullivan, P. P., et al. (2012). A global perspective on Langmuir turbulence in the ocean surface boundary layer. *Geophysical Research Letters*, *39*, L18605. https://doi.org/10.1029/2012GL052932

Bennis, A.-C., Ardhuin, F., & Dumas, F. (2011). On the coupling of wave and three-dimensional circulation models: Choice of theoretical framework, practical implementation and adiabatic tests. *Ocean Modelling*, *40*(3–4), 260–272. https://doi.org/10.1016/j.ocemod.2011.09.003

Booij, N., Ris, R. C., & Holthuijsen, L. H. (1999). A third-generation wave model for coastal regions: 1. Model description and validation. *Journal of Geophysical Research*, *104*(C4), 7649–7666. https://doi.org/10.1029/98JC02622

Brumer, S. E., Zappa, C. J., Blomquist, B. W., Fairall, C. W., Cifuentes-Lorenzen, A., Edson, J. B., et al. (2017). Wave-related Reynolds number parameterizations of CO2 and DMS transfer velocities. *Geophysical Research Letters*, *44*, 9865–9875. https://doi.org/10.1002/2017GL074979

Bunge, L., Ochoa, J., Badan, A., Candela, J., & Sheinbaum, J. (2002). Deep flows in the Yucatan Channel and their relation to changes in the Loop Current extension. *Journal of Geophysical Research*, *107*(C12), 3233, http://doi.org/10.1029/2001JC001256

Cao, Y., Dong, C., Uchiyama, Y., Wang, J., & Yin, X. (2018). Multiple-scale variations of wind-generated waves in the Southern California Bight. *Journal of Geophysical Research: Oceans*, *123*, 9340–9356. https://doi.org/10.1029/2018JC014505

Cardona, Y., & Bracco, A. (2016). Predictability of mesoscale circulation throughout the water column in the Gulf of Mexico. *Deep Sea Research Part II: Topical Studies in Oceanography*, *129*, 332–349. https://doi.org/10.1016/j.dsr2.2014.01.008

Carton, J. A., & Giese, B. S. (2008). A reanalysis of ocean climate using Simple Ocean Data Assimilation (SODA). *Monthly Weather Review*, *136*(8), 2999–3017. https://doi.org/10.1175/2007MWR1978.1

Chelton, D. B., Deszoeke, R. A., Schlax, M. G., El Naggar, K., & Siwertz, N. (1998). Geographical variability of the first baroclinic Rossby radius of deformation. *Journal of Physical Oceanography*, *28*(3), 433–460. https://doi.org/10.1175/1520-0485(1998)028<0433:GVOTFB>2.0.CO;2

Chen, Q., Zhao, H., Hu, K., & Douglass, S. L. (2005). Prediction of wind waves in a shallow estuary. *Journal of Waterway, Port, Coastal, and Ocean Engineering*, *131*(4), 137–148. https://doi.org/10.1061/(ASCE)0733-950X(2005)131:4(137)

Chen, S. S., Zhao, W., Donelan, M. A., & Tolman, H. L. (2013). Directional wind–wave coupling in fully coupled atmosphere–wave–ocean models: Results from CBLAST-Hurricane. *Journal of the Atmospheric Sciences*, *70*(10), 3198–3215. https://doi.org/10.1175/JAS-D-12-0157.1

Clarke, A. J., & Gorder, S. V. (2018). The relationship of near-surface flow, stokes drift and the wind stress. *Journal of Geophysical Research: Oceans*, *123*, 4680–4692. https://doi.org/10.1029/2018JC014102

Collins, C. O. III, Rogers, W. E., Marchenko, A., & Babanin, A. V. (2015). In situ measurements of an energetic wave event in the Arctic marginal ice zone. *Geophysical Research Letters*, *42*, 1863–1870. https://doi.org/10.1002/2015GL063063

D'Asaro, E. A., Thomson, J., Shcherbina, A. Y., Harcourt, R. R., Cronin, M. F., Hemer, M. A., & Fox-Kemper, B. (2014). Quantifying upper ocean turbulence driven by surface waves. *Geophysical Research Letters*, *41*, 102–107. https://doi.org/10.1002/2013GL058193

Deike, L., & Melville, W. K. (2018). Gas transfer by breaking waves. *Geophysical Research Letters*, *45*, 10,482–10,492. https://doi.org/10.1029/2018GL078758

DiMarco, S. F., Nowlin, W. D., & Reid, R. O. (2005). A statistical description of the velocity fields from upper ocean drifters in the Gulf of Mexico. *Geophysical Monograph-American Geophysical Union*, *161*, 101.

Donohue, K. A., Watts, D. R., Hamilton, P., Leben, R., & Kennelly, M. (2016). Loop Current Eddy formation and baroclinic instability. *Dynamics of Atmospheres and Oceans*, *76*, 195–216. https://doi.org/10.1016/j.dynatmoce.2016.01.004

Drennan, W. M., Graber, H. C., Hauser, D., & Quentin, C. (2003). On the wave age dependence of wind stress over pure wind seas. *Journal of Geophysical Research*, *108*(C3), 8062. https://doi.org/10.1029/2000JC000715

Fan, Y., Ginis, I., & Hara, T. (2009). The effect of wind–wave–current interaction on air–sea momentum fluxes and ocean response in tropical cyclones. *Journal of Physical Oceanography*, *39*(4), 1019–1034. https://doi.org/10.1175/2008JPO4066.1

Fan, Y., Jarosz, E., Yu, Z., Rogers, W., Jensen, T., & Liang, J.-H. (2018). Langmuir turbulence in horizontal salinity gradient. *Ocean Modelling*, *129*, 93–103. https://doi.org/10.1016/j.ocemod.2018.07.010

Fan, Y., Lin, S.-J., Griffies, S. M., & Hemer, M. A. (2014). Simulated global swell and wind-sea climate and their responses to anthropogenic climate change at the end of the twenty-first century. *Journal of Climate*, *27*(10), 3516–3536. https://doi.org/10.1175/JCLI-D-13-00198.1

Forristall, G. Z., Schaudt, K. J., & Cooper, C. K. (1992). Evolution and kinematics of a Loop Current eddy in the Gulf of Mexico during 1985. *Journal of Geophysical Research*, *97*(C2), 2173–2184. https://doi.org/10.1029/91JC02905

Gemmrich, J., & Garrett, C. (2012). The signature of inertial and tidal currents in offshore wave records. *Journal of Physical Oceanography*, *42*(6), 1051–1056. https://doi.org/10.1175/JPO-D-12-043.1

Grachev, A. A., & Fairall, C. W. (2001). Upward momentum transfer in the marine boundary layer. *Journal of Physical Oceanography*, *31*(7), 1698–1711. https://doi.org/10.1175/1520-0485(2001)031<1698:UMTITM>2.0.CO;2

Hamilton, P., Fargion, G. S., & Biggs, D. C. (1999). Loop Current eddy paths in the western Gulf of Mexico. *Journal of Physical Oceanography*, *29*(6), 1180–1207. https://doi.org/10.1175/1520-0485(1999)029<1180:LCEPIT>2.0.CO;2

Hanley, K. E., Belcher, S. E., & Sullivan, P. P. (2010). A global climatology of wind–wave interaction. *Journal of Physical Oceanography*, *40*(6), 1263–1282. https://doi.org/10.1175/2010JPO4377.1

Hanson, J. L., Tracy, B. A., Tolman, H. L., & Scott, R. D. (2009). Pacific hindcast performance of three numerical wave models. *Journal of Atmospheric and Oceanic Technology*, *26*(8), 1614–1633. https://doi.org/10.1175/2009JTECHO650.1

Harcourt, R. R. (2015). An improved second-moment closure model of Langmuir turbulence. *Journal of Physical Oceanography*, *45*(1), 84–103. https://doi.org/10.1175/JPO-D-14-0046.1

Harris, D. L. (1966). The wave-driven wind. *Journal of the Atmospheric Sciences*, *23*(6), 688–693. https://doi.org/10.1175/1520-0469(1966)023<0688:TWDW>2.0.CO;2

He, R., & Weisberg, R. H. (2003). A loop current intrusion case study on the West Florida shelf. *Journal of Physical Oceanography*, *33*(2), 465–477. https://doi.org/10.1175/1520-0485(2003)033<0465:ALCICS>2.0.CO;2

Hodges, K., Cobb, A., & Vidale, P. L. (2017). How well are tropical cyclones represented in reanalysis datasets? *Journal of Climate*, *30*(14), 5243–5264. https://doi.org/10.1175/JCLI-D-16-0557.1

Högström, U., Smedman, A., Sahleé, E., Drennan, W. M., Kahma, K. K., Pettersson, H., & Zhang, F. (2009). The atmospheric boundary layer during swell: A field study and interpretation of the turbulent kinetic energy budget for high wave ages. *Journal of the Atmospheric Sciences*, *66*(9), 2764–2779. https://doi.org/10.1175/2009JAS2973.1

Högström, U., Smedman, A.-S., Semedo, A., & Rutgersson, A. (2011). Comments on "A global climatology of wind–wave interaction." *Journal of Physical Oceanography*, *41*(9), 1811–1813. https://doi.org/10.1175/JPO-D-10-05015.1

Holthuijsen, L. H., & Tolman, H. L. (1991). Effects of the Gulf Stream on ocean waves. *Journal of Geophysical Research*, *96*(C7), 12,755–12,771. https://doi.org/10.1029/91JC00901

Holthuijsen, L. H. (2010). *Waves in oceanic and coastal waters*. Cambridge: Cambridge University Press.

Hope, M. E., Westerink, J. J., Kennedy, A. B., Kerr, P. C., Dietrich, J. C., Dawson, C., et al. (2013). Hindcast and validation of Hurricane Ike (2008) waves, forerunner, and storm surge. *Journal of Geophysical Research: Oceans*, *118*, 4424–4460. https://doi.org/10.1002/jgrc.20314

Hu, K., & Chen, Q. (2011). Directional spectra of hurricane-generated waves in the Gulf of Mexico. *Geophysical Research Letters*, *38*, L19608. https://doi.org/10.1029/2011GL049145

Huang, Y., Weisberg, R. H., Zheng, L., & Zijlema, M. (2013). Gulf of Mexico hurricane wave simulations using SWAN: Bulk formula-based drag coefficient sensitivity for Hurricane Ike. *Journal of Geophysical Research: Oceans*, *118*, 3916–3938. https://doi.org/10.1002/jgrc.20283

Kenyon, K. E. (1969). Stokes drift for random gravity waves. *Journal of Geophysical Research*, *74*(28), 6991–6994. https://doi.org/10.1029/JC074i028p06991

Kirby, J. T., & Chen, T.-M. (1989). Surface waves on vertically sheared flows: Approximate dispersion relations. *Journal of Geophysical Research*, *94*(C1), 1013–1027. https://doi.org/10.1029/JC094iC01p01013

Kukulka, T., Plueddemann, A. J., & Sullivan, P. P. (2013). Inhibited upper ocean restratification in non-equilibrium swell conditions. *Geophysical Research Letters*, *40*, 3672–3676. https://doi.org/10.1002/grl.50708

Kukulka, T., Jenkins, R. L., Kirby, J. T., Shi, F., & Scarborough, R. W. (2017). Surface wave dynamics in Delaware Bay and its adjacent coastal shelf. *Journal of Geophysical Research: Oceans*, *122*, 8683–8706. https://doi.org/10.1002/2017JC013370

Kumar, N., Voulgaris, G., Warner, J. C., & Olabarrieta, M. (2012). Implementation of the vortex force formalism in the coupled ocean-atmosphere-wave-sediment transport (COAWST) modeling system for inner shelf and surf zone applications. *Ocean Modelling*, *47*, 65–95. https://doi.org/10.1016/j.ocemod.2012.01.003

Large, W. G., McWilliams, J. C., & Doney, S. C. (1994). Oceanic vertical mixing: A review and a model with a nonlocal boundary layer parameterization. *Reviews of Geophysics*, *32*(4), 363–403. https://doi.org/10.1029/94RG01872

Larson, J., Jacob, R., & Ong, E. (2005). The model coupling toolkit: A new Fortran90 toolkit for building multiphysics parallel coupled models. *The International Journal of High Performance Computing Applications*, *19*(3), 277–292. https://doi.org/10.1177/1094342005056115

Li, Q., Webb, A., Fox-Kemper, B., Craig, A., Danabasoglu, G., Large, W. G., & Vertenstein, M. (2016). Langmuir mixing effects on global climate: WAVEWATCH III in CESM. *Ocean Modelling*, *103*, 145–160. https://doi.org/10.1016/j.ocemod.2015.07.020

Liang, J.-H., Emerson, S. R., D'Asaro, E. A., McNeil, C. L., Harcourt, R. R., Sullivan, P. P., et al. (2017). On the role of sea-state in bubble-mediated air-sea gas flux during a winter storm. *Journal of Geophysical Research: Oceans*, *122*, 2671–2685. https://doi.org/10.1002/2016JC012408

Liang, J.-H., McWilliams, J. C., & Gruber, N. (2009). High-frequency response of the ocean to mountain gap winds in the northeastern tropical Pacific. *Journal of Geophysical Research*, *114*, C12005. https://doi.org/10.1029/2009JC005370

Liang, J.-H., McWilliams, J. C., Kurian, J., Colas, F., Wang, P., & Uchiyama, Y. (2012). Mesoscale variability in the northeastern tropical Pacific: Forcing mechanisms and eddy properties. *Journal of Geophysical Research*, *117*, C07003. https://doi.org/10.1029/2012JC008008

Liang, J.-H., McWilliams, J. C., Sullivan, P. P., & Baschek, B. (2012). Large eddy simulation of the bubbly ocean: New insights on subsurface bubble distribution and bubble-mediated gas transfer. *Journal of Geophysical Research*, *117*, C04002. https://doi.org/10.1029/2011JC007766/full

Liang, J.-H., Wan, X., Rose, K. A., Sullivan, P. P., & McWilliams, J. C. (2018). Horizontal dispersion of buoyant materials in the ocean surface boundary layer. *Journal of Physical Oceanography*, *48*(9), 2103–2125. https://doi.org/10.1175/JPO-D-18-0020.1

Liu, A. K., Jackson, F. C., Walsh, E. J., & Peng, C. Y. (1989). A case study of wave-current interaction near an oceanic front. *Journal of Geophysical Research*, *94*(C11), 16,189–16,200. https://doi.org/10.1029/JC094iC11p16189

Liu, A. K., Peng, C. Y., & Schumacher, J. D. (1994). Wave-current interaction study in the Gulf of Alaska for detection of eddies by synthetic aperture radar. *Journal of Geophysical Research*, *99*(C5), 10,075–10,085. https://doi.org/10.1029/94JC00422

Liu, B., D'Sa, E. J., & Joshi, I. (2019b). Multi-decadal trends and influences on dissolved organic carbon distribution in the Barataria Basin. Louisiana from in-situ and Landsat/MODIS observations. *Remote Sensing of Environment*, *228*, 183–202. https://doi.org/10.1016/j.rse.2019.04.023

Liu, B., D'Sa, E. J., & Joshi, I. D. (2019a). Floodwater impact on Galveston Bay phytoplankton taxonomy, pigment composition and photo-physiological state following Hurricane Harvey from field and ocean color (sentinel-3A OLCI) observations. *Biogeosciences*, *16*(9), 1975–2001. https://doi.org/10.5194/bg-16-1975-2019

Liu, Y., Weisberg, R. H., Lenes, J. M., Zheng, L., Hubbard, K., & Walsh, J. J. (2016). Offshore forcing on the "pressure point" of the West Florida Shelf: Anomalous upwelling and its influence on harmful algal blooms. *Journal of Geophysical Research: Oceans*, *121*, 5501–5515. https://doi.org/10.1002/2016JC011938

Liu, Y., Weisberg, R. H., Vignudelli, S., & Mitchum, G. T. (2016). Patterns of the loop current system and regions of sea surface height variability in the eastern Gulf of Mexico revealed by the self-organizing maps. *Journal of Geophysical Research: Oceans*, *121*, 2347–2366. https://doi.org/10.1002/2015JC011493

Mathiesen, M. (1987). Wave refraction by a current whirl. *Journal of Geophysical Research*, *92*(C4), 3905–3912. https://doi.org/10.1029/JC092iC04p03905

McWilliams, J. C., Restrepo, J. M., & Lane, E. M. (2004). An asymptotic theory for the interaction of waves and currents in coastal waters. *Journal of Fluid Mechanics*, *511*, 135–178. https://doi.org/10.1017/S0022112004009358

McWilliams, J. C., & Sullivan, P. P. (2000). Vertical mixing by Langmuir circulations. *Spill Science & Technology Bulletin*, *6*(3–4), 225–237. https://doi.org/10.1016/S1353-2561(01)00041-X

McWilliams, J. C., Sullivan, P. P., & Moeng, C.-H. (1997). Langmuir turbulence in the ocean. *Journal of Fluid Mechanics*, *334*(1), 1–30. https://doi.org/10.1017/S0022112096004375

Mellor, G. (2003). The three-dimensional current and surface wave equations. *Journal of Physical Oceanography*, *33*(9), 1978–1989. https://doi.org/10.1175/1520-0485(2003)033<1978:TTCASW>2.0.CO;2

Melville, W. K. (1996). The role of surface-wave breaking in air-sea interaction. *Annual Review of Fluid Mechanics*, *28*(1), 279–321. https://doi.org/10.1146/annurev.fl.28.010196.001431

Murphy, A. H., & Epstein, E. S. (1989). Skill scores and correlation coefficients in model verification. *Monthly Weather Review*, *117*(3), 572–582. https://doi.org/10.1175/1520-0493(1989)117<0572:SSACCI>2.0.CO;2

Oey, L.-Y., Ezer, T., & Lee, H.-C. (2013). Loop Current, rings and related circulation in the Gulf of Mexico: A review of numerical models and future challenges. In W. Sturges & A. Lugo-Fernandez (Eds.), *Circulation in the Gulf of Mexico: Observations and models*, *Geophysical Monograph Series* (Vol. 161, pp. 31–56). Washington, DC: American Geophysical Union (AGU). https://doi.org/10.1029/161GM04

Polton, J. A., Lewis, D. M., & Belcher, S. E. (2005). The role of wave-induced Coriolis–Stokes forcing on the wind-driven mixed layer. *Journal of Physical Oceanography*, *35*(4), 444–457. https://doi.org/10.1175/JPO2701.1

Rabe, T., Kukulka, T., Ginis, I., Hara, T., Reichl, B., D'Asaro, E., et al. (2015). Langmuir turbulence under Hurricane Gustav (2008). *Journal of Physical Oceanography*, *45*(3), 657–677. https://doi.org/10.1175/JPO-D-14-0030.1

Rapizo, H., Babanin, A., Gramstad, O., & Ghantous, M. (2014). *Wave refraction on Southern Ocean eddies* (pp. 1–4). Paper presented at Proceedings of the 19th Australasian Fluid Mechanics Conference, Melbourne. http://people.eng.unimelb.edu.au/imarusic/proceedings/19/18.pdf

Reichl, B. G., Wang, D., Hara, T., Ginis, I., & Kukulka, T. (2016). Langmuir turbulence parameterization in tropical cyclone conditions. *Journal of Physical Oceanography*, *46*(3), 863–886. https://doi.org/10.1175/jpo-d-15-0106.1

Rogers, W. E., Kaihatu, J. M., Hsu, L., Jensen, R. E., Dykes, J. D., & Holland, K. T. (2007). Forecasting and hindcasting waves with the SWAN model in the Southern California Bight. *Coastal Engineering*, *54*(1), 1–15. https://doi.org/10.1016/j.coastaleng.2006.06.011

Romero, L., Lenain, L., & Melville, W. K. (2017). Observations of surface wave–current interaction. *Journal of Physical Oceanography*, *47*(3), 615–632. https://doi.org/10.1175/JPO-D-16-0108.1

Rousset, C., & Beal, L. M. (2011). On the seasonal variability of the currents in the Straits of Florida and Yucatan Channel. *Journal of Geophysical Research*, *116*, C08004. https://doi.org/10.1029/2010JC006679

Saha, S., Moorthi, S., Pan, H.-L., Wu, X., Wang, J., Nadiga, S., et al. (2010). The NCEP climate forecast system reanalysis. *Bulletin of the American Meteorological Society*, *91*(8), 1015–1058. https://doi.org/10.1175/2010BAMS3001.1

Semedo, A., Sušelj, K., Rutgersson, A., & Sterl, A. (2011). A global view on the wind sea and swell climate and variability from ERA-40. *Journal of Climate*, *24*(5), 1461–1479. https://doi.org/10.1175/2010JCLI3718.1

Shay, L. K., Goni, G. J., & Black, P. G. (2000). Effects of a warm oceanic feature on Hurricane Opal. *Monthly Weather Review*, *128*(5), 1366–1383. https://doi.org/10.1175/1520-0493(2000)128<1366:EOAWOF>2.0.CO;2

Shchepetkin, A. F., & McWilliams, J. C. (2005). The regional oceanic modeling system (ROMS): A split-explicit, free-surface, topography-following-coordinate oceanic model. *Ocean Modelling*, *9*(4), 347–404. https://doi.org/10.1016/j.ocemod.2004.08.002

Sheng, Y. P., Zhang, Y., & Paramygin, V. A. (2010). Simulation of storm surge, wave, and coastal inundation in the Northeastern Gulf of Mexico region during Hurricane Ivan in 2004. *Ocean Modelling*, *35*(4), 314–331. https://doi.org/10.1016/j.ocemod.2010.09.004

Shi, Q., & Bourassa, M. A. (2019). Coupling ocean currents and waves with wind stress over the gulf stream. *Remote Sensing*, *11*(12), 1476. https://doi.org/10.3390/rs11121476

Sinha, N., Tejada-Martínez, A. E., Akan, C., & Grosch, C. E. (2015). Toward a K-profile parameterization of Langmuir turbulence in shallow coastal shelves. *Journal of Physical Oceanography*, *45*(12), 2869–2895. https://doi.org/10.1175/JPO-D-14-0158.1

Smedman, A., Högström, U., Sahleé, E., Drennan, W. M., Kahma, K. K., Pettersson, H., & Zhang, F. (2009). Observational study of marine atmospheric boundary layer characteristics during swell. *Journal of the Atmospheric Sciences*, *66*(9), 2747–2763. https://doi.org/10.1175/2009JAS2952.1

Smith, A. M., Mather, A. A., Bundy, S. C., Cooper, J. A. G., Guastella, L. A., Ramsay, P. J., & Theron, A. (2010). Contrasting styles of swell-driven coastal erosion: Examples from KwaZulu-Natal, South Africa. *Geological Magazine*, *147*(6), 940–953. https://doi.org/10.1017/S0016756810000361

Smith, W. H., & Sandwell, D. T. (1997). Global sea floor topography from satellite altimetry and ship depth soundings. *Science*, *277*(5334), 1956–1962. https://doi.org/10.1126/science.277.5334.1956

Sorourian, S., Huang, H., Li, C., Justic, D., & Payandeh, A. R. (2020). Wave dynamics near Barataria Bay tidal inlets during spring–summer time. *Ocean Modelling*, *147*, 101553. https://doi.org/10.1016/j.ocemod.2019.101553

Stokes, G. G. (1847). On the theory of oscillatory waves. *Cambridge Transactions*, *8*, 441–455.

Sturges, W., Hoffmann, N. G., & Leben, R. R. (2010). A trigger mechanism for Loop Current ring separations. *Journal of Physical Oceanography*, *40*(5), 900–913. https://doi.org/10.1175/2009JPO4245.1

Sturges, W., & Kenyon, K. E. (2008). Mean flow in the Gulf of Mexico. *Journal of Physical Oceanography*, *38*(7), 1501–1514. https://doi.org/10.1175/2007JPO3802.1

Sturges, W., & Leben, R. (2000). Frequency of ring separations from the Loop Current in the Gulf of Mexico: A revised estimate. *Journal of Physical Oceanography*, *30*(7), 1814–1819. https://doi.org/10.1175/1520-0485(2000)030<1814:FORSFT>2.0.CO;2

Sutherland, P., & Melville, W. K. (2013). Field measurements and scaling of ocean surface wave-breaking statistics. *Geophysical Research Letters*, *40*, 3074–3079. https://doi.org/10.1002/grl.50584

Sutherland, P., & Melville, W. K. (2015). Field measurements of surface and near-surface turbulence in the presence of breaking waves. *Journal of Physical Oceanography*, *45*(4), 943–965. https://doi.org/10.1175/JPO-D-14-0133.1

Terray, E. A., Donelan, M. A., Agrawal, Y. C., Drennan, W. M., Kahma, K. K., Williams, A. J., et al. (1996). Estimates of kinetic energy dissipation under breaking waves. *Journal of Physical Oceanography*, *26*(5), 792–807. https://doi.org/10.1175/1520-0485(1996)026<0792:EOKEDU>2.0.CO;2

The SWAN Team. (2011). *SWAN scientific and technical documentation*. Delft, The Netherlands: Department of Civil Engineering, Delft University of Technology.

The WISE Group (2007). Wave modelling—The state of the art. *Progress in Oceanography*, *75*(4), 603–674. https://doi.org/10.1016/j.pocean.2007.05.005

Tolman, H. L. (2009). User manual and system documentation of WAVEWATCH III TM version 3.14. *Technical Note, MMAB Contribution*, *276*, 220.

Tracy, B., Devaliere, E.-M., Nicolini, T., Tolman, H. L., & Hanson, J. L. (2007). *Wind sea and swell delineation for numerical wave modeling* (pp. 1–12). Paper presented at Proceedings of 10th International Workshop on Wave Hindcasting and Forecasting and Coastal Hazard Symposium. Oahu, HI: U.S. Army Engineer Research & Development Center.

Uchiyama, Y., McWilliams, J. C., & Shchepetkin, A. F. (2010). Wave–current interaction in an oceanic circulation model with a vortex-force formalism: Application to the surf zone. *Ocean Modelling*, *34*(1–2), 16–35. https://doi.org/10.1016/j.ocemod.2010.04.002

Van Roekel, L. P., Fox-Kemper, B., Sullivan, P. P., Hamlington, P. E., & Haney, S. R. (2012). The form and orientation of Langmuir cells for misaligned winds and waves. *Journal of Geophysical Research*, *117*, C05001 Retrieved from. https://doi.org/10.1029/2011JC007516/full

Vázquez De La Cerda, A. M., Reid, R. O., DiMarco, S. F., & Jochens, A. E. (2005). Bay of Campeche circulation: An update. In W. Sturges & A. Lugo-Fernandez (Eds.), *Circulation in the Gulf of Mexico: Observations and models*, *Geophysical Monograph Series* (Vol. 161, pp. 279–293). Washington, DC: American Geophysical Union (AGU). https://doi.org/10.1029/161GM20

Vukovich, F. M. (2007). Climatology of ocean features in the Gulf of Mexico using satellite remote sensing data. *Journal of Physical Oceanography*, *37*(3), 689–707. https://doi.org/10.1175/JPO2989.1

Walker, N. D., Leben, R. R., & Balasubramanian, S. (2005). Hurricane-forced upwelling and chlorophyll *a* enhancement within cold-core cyclones in the Gulf of Mexico. *Geophysical Research Letters*, *32*, L18610. https://doi.org/10.1029/2005GL023716

Walsh, E. J., Wright, C. W., Vandemark, D., Krabill, W. B., Garcia, A. W., Houston, S. H., et al. (2002). Hurricane directional wave spectrum spatial variation at landfall. *Journal of Physical Oceanography*, *32*(6), 1667–1684. https://doi.org/10.1175/1520-0485(2002)032<1667:HDWSSV>2.0.CO;2

Wandres, M., Wijeratne, E. M. S., Cosoli, S., & Pattiaratchi, C. (2017). The effect of the Leeuwin current on offshore surface gravity waves in Southwest Western Australia. *Journal of Geophysical Research: Oceans*, *122*, 9047–9067. https://doi.org/10.1002/2017JC013006

Wang, D. W., Liu, A. K., Peng, C. Y., & Meindl, E. A. (1994). Wave-current interaction near the gulf stream during the surface wave dynamics experiment. *Journal of Geophysical Research*, *99*(C3), 5065–5079. https://doi.org/10.1029/93JC02714

Warner, J. C., Armstrong, B., He, R., & Zambon, J. B. (2010). Development of a coupled ocean–atmosphere–wave–sediment transport (COAWST) modeling system. *Ocean Modelling*, *35*(3), 230–244. https://doi.org/10.1016/j.ocemod.2010.07.010

Webb, A., & Fox-Kemper, B. (2011). Wave spectral moments and Stokes drift estimation. *Ocean Modelling*, *40*(3–4), 273–288. https://doi.org/10.1016/j.ocemod.2011.08.007

Weisberg, R. H., & Liu, Y. (2017). On the Loop Current penetration into the Gulf of Mexico. *Journal of Geophysical Research: Oceans*, *122*, 9679–9694. https://doi.org/10.1002/2017JC013330

Wolf, J., & Prandle, D. (1999). Some observations of wave–current interaction. *Coastal Engineering*, *37*(3–4), 471–485. https://doi.org/10.1016/S0378-3839(99)00039-3

Wright, C. W., Walsh, E. J., Vandemark, D., Krabill, W. B., Garcia, A. W., Houston, S. H., et al. (2001). Hurricane directional wave spectrum spatial variation in the open ocean. *Journal of Physical Oceanography*, *31*(8), 2472–2488. https://doi.org/10.1175/1520-0485(2001)031<2472:HDWSSV>2.0.CO;2

Wu, L., Breivik, Ø., & Rutgersson, A. (2019). Ocean-wave-atmosphere interaction processes in a fully coupled modelling system. *Journal of Advances in Modeling Earth Systems*, *11*, 3852–3874. https://doi.org/10.1029/2019MS001761

Wu, L., Rutgersson, A., Sahlée, E., & Guo Larsén, X. (2016). Swell impact on wind stress and atmospheric mixing in a regional coupled atmosphere-wave model. *Journal of Geophysical Research: Oceans*, *121*, 4633–4648. https://doi.org/10.1002/2015JC011576

Xu, K., Mickey, R. C., Chen, Q., Harris, C. K., Hetland, R. D., Hu, K., & Wang, J. (2016). Shelf sediment transport during hurricanes Katrina and Rita. *Computers & Geosciences*, *90*, 24–39. https://doi.org/10.1016/j.cageo.2015.10.009

Xue, Z., He, R., Fennel, K., Cai, W.-J., Lohrenz, S., & Hopkinson, C. (2013). Modeling ocean circulation and biogeochemical variability in the Gulf of Mexico. *Biogeosciences*, *10*(11), 7219–7234. https://doi.org/10.5194/bg-10-7219-2013